

Lock-exchange gravity currents with a high volume of release propagating over a periodic array of obstacles

TALIA TOKYAY¹, GEORGE CONSTANTINESCU^{1†}
AND ECKART MEIBURG²

¹Department of Civil and Environmental Engineering, IIHR–Hydroscience and Engineering,
The University of Iowa, Iowa City, IA 52242, USA

²Department of Mechanical Engineering, University of California at Santa Barbara,
Santa Barbara, CA 93106-5070, USA

(Received 15 March 2010; revised 11 October 2010; accepted 5 December 2010;
first published online 24 February 2011)

Large eddy simulations are employed to investigate the structure and evolution of a bottom-propagating compositional gravity current in a rectangular horizontal plane channel containing a series of identical large-scale obstacles (dunes and square ribs) at the channel bottom. Simulation results show that below a certain value of the additional drag force per unit streamwise length induced by the bottom obstacles (low drag cases), the gravity current propagating over an array of obstacles transitions to a regime where the average front velocity is close to constant. Past its initial stages, the total kinetic energy, E_k , increases in time proportional to $t^{1/3}$, where t is the time since release. This behaviour is similar to the slumping phase observed for currents propagating over a flat bed, with the exception that in the latter case the temporal increase of E_k during the later stages of the slumping phase is much faster ($E_k \sim t$). Simulation results also show that above certain value of the drag force per unit streamwise length induced by the obstacles (high drag cases), the slumping phase can be very short. In this case, similar to currents propagating in a porous medium, the current transitions to a drag-dominated regime in which the front velocity decays proportionally to t^β , with $\beta = -0.28$, once the discharge of lock fluid at the position of the lock gate becomes close to constant in time.

Key words: gravity currents, separated flows, turbulent mixing

1. Introduction

Gravity currents occur widely in nature. The presence of density differences of only a few per cent can be enough to induce a gravity current that travels over very long distances. Predicting the evolution of turbulent gravity currents is of great interest in many areas of geophysics and engineering, in particular due to their impact on the environment (Fannelóp 1994; Simpson 1997). For example, erosion by gravity currents is one of the main causes for formation of submarine canyons on continental slopes and plays a determinant role in transporting sediments from shallower to

† Email address for correspondence: sconstan@engineering.uiowa.edu

deeper regions in water environments (Meiburg & Kneller 2010). The propagation of gravity currents is often accompanied by disastrous damage (e.g. powder-snow avalanches in mountainous terrains).

The surface over which gravity currents propagate in the environment is often not smooth. The presence of bedforms (e.g. dunes, ripples at the bottom of rivers and oceans) and topographic bumps, of a vegetation layer, or of an array of obstacles leads to an additional net drag force which slows down the gravity current with respect to the case when it propagates over a smooth surface (Hatcher, Hogg & Woods 2000). For example, arrays of obstacles are often used as protective measures on hilly terrains and on the skirts of mountains to stop or slow down gravity currents in the form of powder-snow avalanches (Hopfinger 1983). Even if they do not arrest the flow, the retarding obstacles reduce the impact of the avalanche on buildings situated downstream of the obstacles. The presence of an array of obstacles that play the role of roughness elements can slow down the gravity current and substantially modify its capacity to entrain sediment with respect to the case of a current propagating over a flat surface.

The effects of obstacles on the flow within a turbulent bottom-propagating gravity current are, in many regards, similar to those observed for turbulent constant-density flows propagating over rough surfaces (Jimenez 2004). In both cases, the presence of large-scale bedforms or obstacles at the channel bottom provides an additional mechanism for energy dissipation. In the case of constant density flows, the effects of the presence of arrays of obstacles of various shapes or bedforms at the bottom of a channel are fairly well understood (e.g. Djenidi, Elavaransan & Antonia 1999; Ikeda & Durbin 2002; Leonardi *et al.* 2003; de Angelis, Lombardy & Banerjee 1997). Some of these numerical and experimental studies provide a detailed discussion of the effects of the spacing, shape and size of the roughness elements on the mean flow and turbulence structure in straight horizontal channels.

The case of a gravity current propagating into a straight channel with a flat horizontal bed has also received a significant amount of attention, especially for gravity currents in lock-exchange configurations. Numerous experimental (e.g. Huppert & Simpson 1980; Hallworth *et al.* 1996; Kneller, Bennett & McCaffrey 1999; Shin, Dalziel & Linden 2004) and numerical (e.g. Härtel, Meiburg & Necker 2000; Necker *et al.* 2005; Cantero *et al.* 2007; Hallez & Magnaudet 2008, 2009; Ooi, Constantinescu & Weber 2009) studies were conducted to understand the structure of the current and to measure the time variation of the front velocity during the different phases of the propagation of the current and other quantities that characterize the evolution of the current.

Another category of relevant studies deals with the interaction between gravity currents and isolated surface-mounted obstacles or ridges. Armi (1986) proposed a comprehensive theoretical framework for the study of two-layer flows interacting with an isolated bottom-mounted obstacle characterized by a long lee side and a smooth variation in the surface slope. By parametrizing the flows in terms of the internal Froude number for each layer, Armi (1986) investigated the conditions for which the subcritical two-layer flow ahead of the obstacle becomes supercritical past the crest of the obstacle inside the bottom layer in which the higher density flow is strongly accelerated. His study also discussed the physics of the transition of the flow inside the bottom layer to subcritical conditions at larger distances from the obstacle. Experiments (e.g. Pawlak & Armi 2000) have shown that the increased shear between the two layers induces the generation of large Kelvin–Helmholtz (KH) interfacial vortices on the leeward side of the obstacle. This results in the formation of an

intermediate layer of mixed fluid downstream of the crest of the obstacle. Pawlak & Armi (2000) provided a detailed description of the structure and development of the mixing layer that eventually leads to the formation of a steady downslope current of mixed fluid. Analytical models, based on the shallow flow equations that take into account the turbulent mixing between the layers, have been proposed to predict the streamwise variation of the flow and depth of the intermediate mixing layer region (e.g. Liapidevskii 2004).

The case considered in the present study is in many regards different. The main difference is that, as the front reaches the next obstacle in the series, a backward-propagating hydraulic jump is generated. The quasi-steady structure of the three-layer flow observed at large distances behind the front is, to a large degree, determined by the passage of the backward-propagating jumps. As the rib and dune obstacles considered in the present study do not have a long lee side that smoothly connects the top/crest with the lower part of the bottom, the development of the mixing layer is expected to be different. Also, for the higher-rank obstacles, the flow within the bottom layer is far from homogeneous. Still, as the present results will show, some of the fundamental physics observed in the aforementioned studies of flow past isolated obstacles is also present in the case of a current propagating past an array of ribs or dunes. The most important aspect is that if the incoming flow conditions and obstacle dimensions are such that the bottom current transitions to the supercritical regime past the crest of the obstacle, an intermediate region of strongly mixed fluid develops downstream of the crest/top of the obstacle that was overtaken by the front of the current. The mixing in this region is driven by the strong acceleration of the fluid within the bottom higher-density layer, which results in the formation of KH vortices at the bottom interface of the layer of mixed fluid. In the classification proposed by Liapidevskii (2004), this case corresponds to the scenario where the flow within the bottom layer resembles a surface-jet flow developing on the lee side of the obstacle. Results of our study will show that a strong jet-like flow develops past the top of the obstacles.

Several studies (e.g. Rottman *et al.* 1985; Lane-Serff, Beal & Hadfield 1995) proposed analytical models based on shallow water theory to determine the fraction of the gravity current flow that is convected over an isolated obstacle, the speed of the reflected jump and the depth of the reflected flow. A similar model that also estimates the height and the speed of the current downstream of the surface-mounted obstacle was proposed by Gonzalez-Juez & Meiburg (2009). Gonzalez-Juez, Meiburg & Constantinescu (2009) and Gonzalez-Juez *et al.* (2010) used results from highly resolved large eddy simulation (LES) to study changes in the structure of the gravity current as it interacts with isolated obstacles mounted on a flat bed surface or situated at a small distance from the flat bed (e.g. pipelines). These studies provided quantitative insight into the physical mechanisms generating the drag forces on the obstacle during the different stages of the interaction between the current and the obstacle.

The case of a gravity current propagating over a bed containing an array of large-scale roughness elements has received much less attention. Hopfinger (1983) and Johanneson *et al.* (1996) provided a discussion of dilute powder-snow avalanches and their interaction with an array of retarding mounds. However, to our knowledge, no experimental studies have been conducted to date that aim at unraveling the fundamental physics of bottom-propagating gravity currents over arrays of large-scale obstacles in an unstratified environment. Some indirect knowledge is available from

experimental studies of lock-exchange gravity currents propagating in a porous medium in a horizontal bed channel (e.g. Hatcher *et al.* 2000; Tanino, Nepf & Kulis 2005). All these experimental studies were conducted with arrays of bed-mounted vertical cylinders occupying the whole depth of the channel.

Hatcher *et al.* (2000) developed a theoretical model for gravity currents propagating into a porous medium of uniform porosity in which the presence of the obstacles is modelled by a uniform drag force proportional to the square of the velocity and inversely proportional to the mean length scale of the obstacle. The model is based on depth-averaged single-layer shallow-water theory and considers the case of a gravity current propagating into an extensive region containing obstacles. The similarity solutions obtained by Hatcher *et al.* (2000) described the motions of gravity currents following finite volume and continuous releases of heavier lock fluid. In particular, they found that for finite (constant) volume instantaneous releases, an intermediate buoyancy-turbulent drag flow regime may be present in between the buoyancy-inertia and viscous-buoyancy self-similar regimes. In this intermediate flow regime, the main forces that drive the evolution of the current are the turbulent drag and the buoyancy forces. Hatcher *et al.* (2000) found that during the turbulent drag-dominated regime, the front velocity, U_f , is proportional to $t^{-1/2}$ rather than $t^{-1/3}$, as is the case for the buoyancy-inertia regime. In the case of a continuous release with a total volume of lock fluid that increases linearly with time, the model predicts that $U_f \sim t^{-1/4}$ over the drag-dominated regime.

Tanino *et al.* (2005) performed an experimental study of gravity currents in lock exchange configurations with a large volume of release. The currents propagated through a random array of rigid bottom-mounted vertical cylinders. They found that the current transitions from the constant velocity slumping phase to a turbulent drag-dominated regime in which the front velocity decreases with time. A theoretical model was developed to predict the temporal variation of the front velocity during the drag-dominated regime in which the shape of the interface is triangular.

In the above cases, the drag force induced by the cylinders acts over the whole height of the gravity current. In contrast, in the case considered in the present study, in which the gravity currents propagate over roughness elements with a maximum height that is significantly lower than that of the current, the additional drag force induced by the obstacles acts only over the lower part of the bottom-propagating current. This may result in important differences between the two cases in terms of the flow and turbulence structure within the body of the gravity current, the shape of the interface, the temporal evolution of the front velocity, etc.

The numerical study of Ozgokmen *et al.* (2004) was the first to consider the propagation of a gravity current over a rough bottom. They employed non-hydrostatic simulations to explore the influence of sloping, rough seafloor topographies on the entrainment rates of overflow currents propagating in an unstratified environment. Their focus was on potentially self-similar seafloor features with length scales $O(1\text{ m}–100\text{ km})$, which are modelled by sinusoidal perturbations. The simulations were conducted at field scale conditions with constant but unequal viscosities/diffusivities in the horizontal and vertical directions. This line of investigation was further extended by Ozgokmen & Fisher (2008) for the case of a saline current propagating into a temperature-stratified ambient fluid. The study focused on the temporal changes in the structure, entrainment and the front propagation speed of the current as a function of the bottom roughness once the nose starts lifting from the bottom and the current

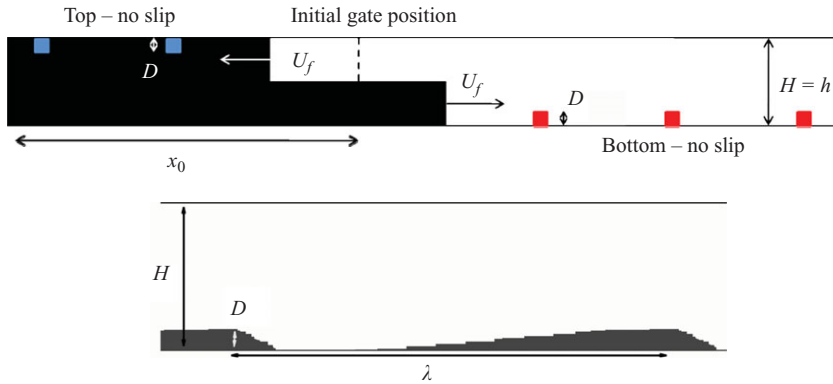


FIGURE 1. (Colour online available at journals.cambridge.org/flm) Sketch of a full-depth lock-exchange flow. The gate is positioned far from the extremities of the channel ($x_0/H \gg 1$). The top and bottom no-slip walls are horizontal. Also shown is the shape of the bed surface used in the simulations with dunes.

propagates at the level of neutral buoyancy. The authors presented results on the front velocity for different levels of stratification of the ambient fluid and amplitudes of the seafloor sinusoidal bumps. Furthermore, the authors evaluated the drag exerted on the overflow current by the bottom roughness, drawing attention to the role of separation and the resulting form drag. In contrast, the present investigation addresses the dynamics of gravity currents flowing over a non-sloping, smooth boundary with a series of localized obstacles during the slumping and drag-dominated regimes.

In the present numerical study, we consider the case of compositional Boussinesq currents. The case of lock-exchange currents with a full-depth of release is considered, in which the height of the lock-gate opening, h , is equal to the channel height, H (figure 1). The initial volume of release is large enough ($R = h/x_0 \ll 1$) such that no interactions occur between the forward- and backward-propagating currents and the channel endwalls during the simulations. LES are conducted at Reynolds numbers defined with the front velocity and the head height that are sufficiently high ($>10^4$) for the flow behind the front to be strongly turbulent, at least during the slumping phase (Ooi *et al.* 2009).

The bottom-propagating current advances over a flat horizontal bed or over an array of identical two-dimensional (2-D) obstacles in the form of square ribs or dunes. The 2-D dunes are representative of bedforms present at the bottom of rivers and oceans while the 2-D ribs resemble the retarding devices used to slow down snow avalanches. At a more fundamental level, the main difference between the two types of obstacles is the degree of bluntness of the obstacle, given by the degree of inclination of its upslope face with the bed. In the case of ribs, the upslope face is perpendicular to the channel bed. This increases the form drag as compared with cases when the change in elevation between the lowest and highest levels of the obstacle is gradual (e.g. dunes). In all the simulations, the mean (background) slope of the bottom surface is equal to zero and the height of the obstacles ($D = 0.15H$) is less than the height of the gravity current, but sufficiently high for the form drag to be much larger than the friction drag. The goal of the present investigation is to study the effects of the shape and spacing of the large-scale roughness elements on the evolution and structure of a lock-exchange compositional current propagating over a horizontal bed and to

compare with the widely studied case of a current propagating over a flat smooth bed.

Results from three-dimensional (3-D) LES capable of capturing the large-scale flow instabilities and dynamics of the turbulent structures are used to clarify the flow physics and answer several important questions related to the propagation of gravity currents over a rough bed. The first question is whether, similar to the case of a current propagating over a smooth flat surface, a slumping phase is present in which the front velocity is constant. If so, how does the front velocity vary with the shape of the obstacle and with the Reynolds number? How do the obstacles affect the structure of the flow in the head and tail regions during the slumping phase? How is the energy balance affected as compared with the case of a current propagating over a smooth surface? Are scale effects important between the Reynolds numbers at which most laboratory experiments are conducted and Reynolds numbers that are closer to field conditions? What is the effect of the obstacles on the total drag force acting on the current and how is the degree of bluntness of the obstacles affecting the total drag force? How does the presence of the obstacles modify mixing and entrainment with respect to the case of a horizontal smooth bed?

The main effect of the bottom-mounted obstacles on the flow is to increase the drag force acting on the current. On the basis of studies of gravity currents propagating in a porous medium, we know that if the drag force is large enough, the gravity current will transition from the slumping phase to a turbulent drag-dominated regime in which the front velocity decays with time. Supposing that the spatial distribution of the drag force acting on the current is of secondary importance, one expects that currents propagating over bottom-mounted obstacles will reach a similar regime. The transition to the drag-dominated regime is expected to depend primarily on the total drag force per unit streamwise length. If such a regime is reached for gravity currents propagating over bottom-mounted obstacles, one important question is how do the front velocity and kinetic energy vary with time? Do the theoretical models developed for gravity currents propagating in a porous medium still apply? Is the structure of a gravity current propagating over a rough bed different during the slumping phase and the drag-dominated regime?

The numerical method, boundary conditions and the matrix of the LES are discussed in §2. Section 3 analyses the temporal variation of the front velocity and the different regimes observed in the evolution of currents propagating over a rough bed as a function of the shape and wavelength of the obstacles and the Reynolds number. Section 4 focuses on analysing the flow structure of gravity currents propagating over obstacles for cases where the total drag force per unit streamwise length is relatively low, such that the current propagates with constant mean front velocity for a relatively long time period. These cases allow a direct comparison with the case of a gravity current propagating over a smooth flat surface during the slumping phase. The section also discusses the flow structure of a gravity current propagating over densely spaced ribs, after the transition to the drag-dominated regime has ended. Section 5 discusses the energy budget and reveals different regimes for the variation of the total kinetic energy with time or with the front position for gravity currents propagating over obstacles. Section 6 discusses how the presence of obstacles in the form of ribs and dunes changes the spatial distribution of the local dissipation rate with respect to the flat-bed case for lock-exchange flows, in which the slumping phase lasts for a relatively large time. Section 7 discusses the temporal evolution of the drag forces. Mixing and entrainment are analysed in §8. Section 9 summarizes the main findings and conclusions.

2. Description of numerical model and simulations

The filtered Navier–Stokes equations and the advection–diffusion equation for the concentration \bar{C} are made dimensionless using the channel depth, H , and the buoyancy velocity, $u_b = \sqrt{g'H}$, ($g' = g(\rho_{max} - \rho_{min})/\rho_{max}$, where ρ_{max} and ρ_{min} are, respectively, the maximum and minimum initial densities in the domain, and g is the gravitational acceleration):

$$\frac{\partial u_i}{\partial x_i} = 0, \quad (2.1)$$

$$\frac{\partial u_i}{\partial t} + \frac{\partial(u_i u_k)}{\partial x_k} = -\frac{\partial p}{\partial x_i} + \frac{\partial}{\partial x_k} \left[\left(\frac{1}{Re} + \nu_{SGS} \right) \left(\frac{\partial u_i}{\partial x_k} + \frac{\partial u_k}{\partial x_i} \right) \right] - C \delta_{i2}, \quad (2.2)$$

$$\frac{\partial C}{\partial t} + \frac{\partial(C u_k)}{\partial x_k} = \frac{\partial}{\partial x_k} \left(\left(\frac{1}{ReSc} + \alpha_{SGS} \right) \frac{\partial C}{\partial x_k} \right), \quad (2.3)$$

where p and u_i are respectively the dimensionless pressure and the Cartesian velocity component in the i -direction. The dimensionless concentration is defined as $C = (\bar{C} - \bar{C}_{min})/(\bar{C}_{max} - \bar{C}_{min})$, where \bar{C}_{max} and \bar{C}_{min} are the maximum and minimum initial concentrations in the domain. Here C is linearly related to the density ρ . The coordinates in the three directions are denoted either (x_1, x_2, x_3) in index notation, or (x, y, z) . The vertical direction is y ($i=2$, in index notation). The time scale is $t_0 = H/u_b$.

The non-dimensional equations contain two flow parameters. The Reynolds number, $Re = u_b H/\nu$, is the ratio between inertial and viscous forces. The Schmidt number, Sc , is the ratio of the molecular viscosity, ν , to the molecular diffusivity, κ . The SGS viscosity (ν_{SGS}) and SGS diffusivity (α_{SGS}) in (2.2) and (2.3) are calculated using a dynamic procedure (Pierce & Moin 2001). No assumptions are needed for the value of the turbulent Schmidt number, as the dynamic procedure directly estimates the value of the SGS diffusivity based on the resolved velocity and concentration fields. The governing equations are integrated through the viscous sublayer.

The finite-volume LES solver (Pierce & Moin 2001) solves the conservative form of the Navier–Stokes equations on non-uniform Cartesian meshes. A semi-implicit iterative method that employs a staggered conservative space–time discretization is used to advance the equations in time, while ensuring second-order accuracy in both space and time. To ensure that the continuity (2.1) is satisfied, a Poisson equation is solved for the pressure using a multigrid approach. The algorithm discretely conserves energy (Mahesh, Constantinescu & Moin 2004), which ensures robustness at high Reynolds numbers without using dissipative schemes to discretize the Navier–Stokes equations. All operators are discretized using central discretizations, except the convective term in the advection–diffusion equation solved for the dimensionless concentration, for which the quadratic upwind interpolation for convective kinematics (QUICK) scheme is used.

Validation of the incompressible flow solver for constant density turbulent flows and for stratified flows (e.g. intrusive gravity currents and gravity currents propagating over a flat smooth bed) has been discussed by Pierce & Moin (2001, 2004), Chang, Constantinescu & Park (2006, 2007), Ooi, Constantinescu & Weber (2007a,b) and Ooi *et al.* (2009). Gonzalez-Juez *et al.* (2009) successfully reproduced the measured (Ermanyuk & Gavrilov 2005a,b) time-varying drag and lift coefficients of gravity current flows over circular and square cylinders separated by a gap from the bottom wall.

Case	Re	Obstacle	D/H	λ/H	Position of the obstacles
LR-F	47 800	–	–	–	–
LR-D15	47 800	Dune	0.15	3	$x/H = 5, 8, 11, 14, 17$
LR-R15	47 800	Rib	0.15	3	$x/H = 5, 8, 11, 14, 17$
HR-F	1 000 000	–	–	–	–
HR-D15	1 000 000	Dune	0.15	3	$x/H = 5, 8, 11, 14, 17$
HR-R15	1 000 000	Rib	0.15	3	$x/H = 5, 8, 11, 14, 17$
LR-R15-HD	47 800	Rib	0.15	1	$x/H = 5, 6, \dots, 26, 27$

TABLE 1. Main parameters of the simulations.

The matrix of the simulation parameters is presented in table 1. The LES conducted at $Re = 47\,800$ are denoted LR. The LES conducted at $Re = 10^6$ are denoted HR. The presence of a flat bed, 2-D dunes or 2-D ribs is indicated by letter F, D or R in the notation, respectively. The non-dimensional height of the ribs or dunes, $D/H \times 100$, is indicated by a number. For example, LR-R15 refers to the simulation of the flow past an array of 2-D ribs of height $0.15H$ conducted at $Re = 47\,800$. With the exception of case LR-R15-HD, the wavelength λ between successive obstacles is equal to $3H$ in all the simulations.

The initial lock-gate position is at $x/H = 0$. The obstacles are positioned on the bottom surface in the region with $x/H > 0$ and on the top surface in the region with $x/H < 0$. The centre of each rib is situated at the location of the crest of the corresponding dune. Their streamwise positions along the top and bottom walls are given in table 1. The channel geometry and boundary conditions are such that the propagation of the heavier and lighter Boussinesq currents is close to anti-symmetrical. Though the initial random perturbations induce differences in the eddies developing on the two sides of the lock gate (see also discussion in Bonometti, Balachandar & Magnaudet 2008), the large-scale features observed in the distributions of the relevant variables (e.g. velocity and dissipation rate) at a given time are sufficiently close to allow focusing the discussion of the results on the evolution of the heavier (forward-propagating in figure 1) current.

The effect of the shape of the obstacles is studied by considering obstacles in the form of square ribs and dunes, respectively (figure 1). In the base case, their height is $D = 0.15H$ and the wavelength is $\lambda = 3H$ ($\lambda/D = 20$). This spacing corresponds to the k -type roughness regime (e.g. see Jimenez 2004) in which the equivalent sand roughness is proportional to the dimension (height) of the roughness elements (obstacles). In the case of k -type roughness, the heavier fluid flows past the crest of each obstacle and then reattaches to the lower part of the bed before starting to interact with the next obstacle in the series. This is the relevant regime for most practical applications in geosciences. The shape of the dunes is taken from the experiment of Mierlo & de Ruiter (1988), which focused on typical dunes observed in small- and medium-size rivers.

Scale effects are discussed based on comparisons of simulations with flat bed, dunes and ribs conducted at $Re = 47\,800$ and $Re = 10^6$. In the latter case, the Reynolds number is sufficiently high for the current to approach the inviscid state. The Reynolds number in the HR simulations is within the lower part of the range of Reynolds numbers observed in the field (e.g. gravity currents in small rivers). A comparison of simulations LR-R15 ($\lambda = 3H$) and LR-R15-HD ($\lambda = H$) allows one to study the effect of increasing, by a factor of three, the drag force per unit streamwise length on the evolution of the gravity current.

The number of grid points was $4232 \times 48 \times 152$ in the streamwise (domain length $L_1 = 41H$), spanwise (domain width $L_3 = H$) and vertical (domain height $L_2 = H$) directions, respectively. Away from the walls, the grid spacing in the three directions was $0.01H$ – $0.02H$. To resolve the viscous sublayer, the grid spacing in the vertical direction was reduced to $0.002H$ near the top and bottom boundaries in the simulations conducted at $Re = 47\,800$. The grid spacing was also reduced close to the lateral and top surfaces of the ribs. A grid spacing of $0.002H$ in the wall-normal direction corresponds to about one wall unit. This is sufficient to resolve the viscous sublayer if the flow behind the front is assumed to be fully developed and, thus, to avoid the use of wall functions. In the simulations conducted at $Re = 10^6$, the grid spacing at the top and bottom boundaries was around $0.0007H$ in the wall-normal direction. The grid spacing away from the walls was of the order of 100 non-dimensional wall units. This is similar to the one used in an LES of a gravity current with a small volume of release conducted at $Re = 10^6$, which is part of the study conducted by Ooi *et al.* (2009) using the same code. The 3-D LES of Ooi *et al.* (2009) correctly predicted the change in the front speed with the Reynolds number during the slumping phase and a front speed decrease proportional to t^β over the buoyancy–inertia phase, with the constant β approaching the theoretical value of $-1/3$ as the current gets close to the inviscid limit ($Re \cong 10^6$).

No-slip boundary conditions were used for the velocity at the top and bottom boundaries. Härtel *et al.* (2000), Necker *et al.* (2002, 2005), Cantero *et al.* (2007) and Ooi *et al.* (2009) did not find a significant effect of the Schmidt number on the solution if $1 < Sc < 1000$. Simulations in the present study assumed $Sc = 600$, which corresponds to the saline diffusion in water. A zero normal gradient was imposed for the concentration at the top, bottom and endwall boundaries. The flow was assumed to be periodic in the spanwise direction. Thus, the present study considers only gravity currents of large relative width, which are particularly relevant for geoscience applications. The effect of the sidewalls was studied by Hallez & Magnaudet (2008). The flow field was initialized with fluid at rest. A random disturbance was applied on the concentration field in the lock-gate region to accelerate the growth of 3-D instabilities. The time step was $0.001t_0$.

3. Front velocity

Previous experimental and numerical investigations (e.g. see Rottman & Simpson 1983; Shin *et al.* 2004; Ooi *et al.* 2009) showed that, after a short initial acceleration phase, lock-exchange gravity currents propagating over a flat smooth surface reach a regime in which the front velocity, U_f , is close to constant (slumping phase).

Figure 2 shows the temporal evolution of the front position x_f/H for the heavier current in the simulations conducted with a flat bed and with an array of obstacles ($D = 0.15H$, $\lambda = 3H$), at $Re = 47\,800$ and $Re = 10^6$. The front position corresponds to the nose of the current inferred from the spanwise-averaged concentration field ($C = 0.05$).

As expected, in the flat-bed cases, after the end of the initial acceleration phase ($t/t_0 = 3.5$), the front trajectory can be well approximated by a line of constant slope, until the end of the simulations. The non-dimensional front velocity, $\bar{U}_f = U_f/u_b$, during the slumping phase is 0.45 and 0.49 for cases LR-F and HR-F, respectively. These values are in very good agreement with those inferred from experiments of high-Reynolds-number currents propagating over a flat smooth bed (e.g. Keulegan 1957; Shin *et al.* 2004). For example, Keulegan (1957) found $\bar{U}_f = 0.48$ for currents

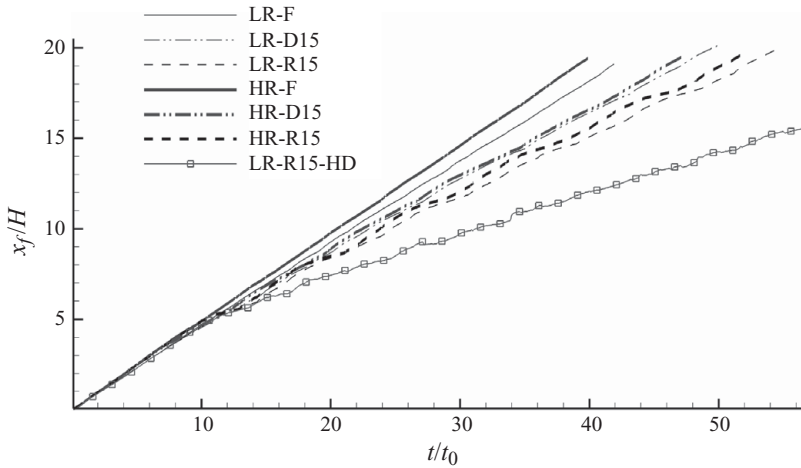


FIGURE 2. Time variation of the non-dimensional position of the front, x_f/H , as a function of the non-dimensional time t/t_0 in the low- (LR) and high- (HR) Reynolds-number simulations with a flat bed and with obstacles ($D=0.15H$ and $\lambda=3H$). The front trajectories show that a regime in which the mean front velocity is constant in time is reached in all simulations. The solid grey line with squares shows the front trajectory for case LR-R15-HD in which x_f increases proportionally to t^α ($\alpha=0.72$) in the later stages of the evolution of the current (see also figure 3a).

with front Reynolds numbers ($Re_f = U_f(H/2)/\nu$) around 150 000. The front velocity in the HR-F simulation, in which $Re_f = 248\,000$, is very close to the theoretical value of 0.5 (half-depth solution) obtained by Benjamin (1968) for an energy-conserving inviscid current.

The presence of ribs or dunes slows down the advancement of the front compared with the flat-bed case. In figure 2, the front trajectories are very close until the front approaches the first obstacle at $x=5H$. The trajectories start diverging for $t/t_0 > 10$. Still, for $t/t_0 > 16$, the mean slope of the trajectory can be considered, to a good approximation, constant in the LR-R15 and LR-D15 simulations. This indicates that under certain conditions (e.g. depending on the values of D/H and λ/H , the shape of the obstacles) a slumping phase in which the front velocity is approximately constant is also present for gravity currents propagating over a rough bed.

In the simulations with a rough bed, the slope of the front trajectory is subject to larger temporal variations as compared with those observed in the simulations with a smooth bed. This is because the front is decelerating as it approaches the crest of each dune or the upstream face of each rib, due to the adverse pressure gradients induced by the inclined upstream surface of the obstacle. The potential energy increases during the time the head rises above the top of the obstacle, at the expense of the head losing some of its kinetic energy. In the case of ribs, there is an additional increase in the potential energy due to the splash of higher density fluid forming as a result of the impact between the head of the current and a bluff obstacle. This is why the slope of the front trajectory is subject to larger amplitude temporal variations in the simulations involving obstacles with a high degree of bluntness (ribs). The front velocity increases above the mean value during the time the head is projected downwards, as it passes the crest of the dune or the top of the rib.

The mean values of \bar{U}_f estimated based on the mean slope of the front trajectory ($t/t_0 > 20$) in figure 2 are 0.34 and 0.4 for cases LR-R15 and LR-D15, respectively.

An analysis of the simulation results shows that the mean value obtained from the front trajectory is in very good agreement with estimates of the mean front velocity based on the time it takes the front to advance between two successive obstacles. In the latter case, present results show that, past the second obstacle, the mean front velocity in between two successive obstacles is close to independent of the rank of the obstacle in the series, and oscillates around the mean value inferred from the front trajectory (the difference is less than 3%). The mean front velocity in the LR-D15 and LR-R15 simulations is, respectively, 12% and 24%, lower than the value ($\bar{U}_f = 0.45$) computed for the flat-bed case. The additional form drag induced by the presence of the obstacles is the main cause for the reduction of the mean value of the front velocity during the slumping phase in cases LR-R15 and LR-D15 as compared with case LR-F. For obstacles of identical heights, the form drag is larger for obstacles with a higher degree of bluntness. The presence of a slumping phase is dependent on the total drag per unit streamwise length acting on the current. Similar simulations performed in our group with obstacles of height comparable or larger than that of the incoming current ($D > 0.3H$, $\lambda = 3H$) showed that the mean front velocity in between two successive obstacles starts decaying with the rank of the obstacles.

As opposed to the flat-bed simulations in which there is an increase of about 10% in the front velocity between $Re = 47\,800$ and $Re = 10^6$, the mean front velocity is much less sensitive to the Reynolds number in the simulations with obstacles of height $D = 0.15H$ and wavelength $\lambda = 3H$, regardless of the degree of bluntness of the obstacles. The mean front velocity ($\bar{U}_f = 0.4$ for $Re = 10^6$ and $\bar{U}_f = 0.4$ for $Re = 47\,800$) is nearly independent of the Reynolds number in the simulations with dunes. In the simulations with ribs, a small increase in the front velocity is observed between the LR-R15 ($\bar{U}_f = 0.34$) and HR-R15 ($\bar{U}_f = 0.36$) cases. Scale effects are relatively minor in terms of the temporal evolution of the front position for gravity currents propagating over a series of dunes or ribs. Thus, as opposed to the flat-bed case, experiments conducted with $Re_f = U_f(H/2)/\nu \cong 10\,000$ ($Re \cong 50\,000$) should be fairly representative of field conditions, at least as far as the front velocity is concerned.

Next, the temporal variation of the front velocity in a case with more densely spaced ribs with $\lambda = H$ (LR-R15-HD) is analysed. The smaller spacing means that the effect of the drag force on the current will be proportionally larger over the same streamwise distance. The number of ribs on each side of the lock is equal to 22, compared with only 5 in the LR-R15 case, and the channel is longer. The number of mesh point in the streamwise direction was also increased to maintain the same flow resolution as in the other simulations.

In the case of constant density flows, a d -type roughness regime (Jimenez 2004) is expected to be observed for roughness elements with $D/\lambda = 0.15$ (case LR-R15-HD). The d -type roughness regime is present when the shear layer forming at the top/crest of an obstacle or bedform does not reattach to the lower part of the channel bottom in between that obstacle and the next obstacle in the series. Present results show that in the case of a gravity current flow, the head reattaches to the bottom of the channel before reaching the next rib (e.g. at about $3D$ or 0.5λ upstream of the next rib in case LR-R15-HD). Thus, in the case of gravity currents, the conditions considered in case LR-R15-HD correspond to a k -type roughness regime (Jimenez 2004). The larger drag force per unit length is expected to slow down the current with respect to the LR-R15 simulation. However, two important questions are whether or not the slumping phase will be present as the current propagates over the obstacles,

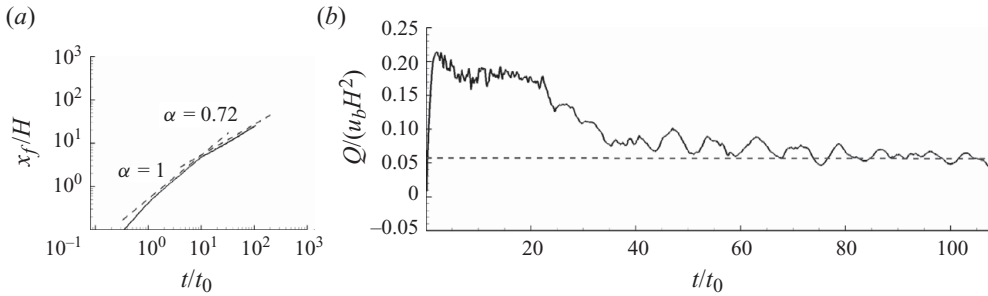


FIGURE 3. (a) Time variation of the non-dimensional position of the front, x_f/H , as a function of the non-dimensional time, t/t_0 , in the LR-R15-HD simulation ($D=0.15H$ and $\lambda=H$) plotted in the log–log scale. The dashed line shows a best fit of the form $x_f = ct^\alpha$. Also shown in (b) is the time variation of the flux of the lock fluid, $Q/(u_b H^2)$, at the position of the gate ($x/H=0$). The figure shows that a regime in which x_f increases proportionally to t^α ($\alpha=0.72$) is reached in case LR-R15-HD after Q becomes close to constant.

and whether for a gravity current with a large volume of release ($R = h/x_0 \ll 1$) this slumping phase will be followed by a turbulent-drag-dominated regime in which the front velocity decays in time.

In case LR-R15-HD, the current transitions to the slumping phase ($\bar{U}_f = 0.45$ over the region where $\alpha = 1$ in figure 3a) before it starts interacting with the first rib in the series ($t \sim 10t_0$). After the current overtakes the first few ribs, the front velocity is close to $0.28u_b$, which is significantly smaller than the front velocity ($U_f = 0.34u_b$) computed during the slumping phase in case LR-R15. However, while propagating over the ribs, the front velocity never reaches a regime where it is constant over time. Rather, the time interval it takes the current to travel to the next rib in the series starts increasing and the associated front velocity starts decaying with the rank of the rib for $t > 10t_0$. For example, at $t = 50t_0$, $U_f \sim 0.22u_b$, while at $t = 90t_0$, $U_f = 0.19u_b$.

The log–log plot in figure 3(a) shows that, after the current overtakes the first couple of ribs in the series ($t > 20t_0$), $x_f(t) \sim t^\alpha$ with $\alpha = 0.72$. This value is close to the value ($\alpha = 0.75$) given by the analytical model of Hatcher *et al.* (2000) for the case of gravity currents with a volume of lock fluid that increases linearly with time. This comparison is justified, as the discharge of the lock fluid at the gate position is close to constant for $t > 35t_0$ (figure 3b). This means that the increase of the volume of lock fluid in the region with $x/H > 0$ is close to linear. The presence of a regime in which $x_f(t) \sim t^\alpha$ with $\alpha < 1$ means that a drag-dominated (nonlinear) regime is present in case LR-R15-HD. In contrast to the experiments of Tanino *et al.* (2005), the shape of the interface away from the front is not linear. This is expected, as the linear shape of the interface in the experiments of Tanino *et al.* (2005) is due to the presence of uniformly distributed obstacles over the whole height of the channel, which is not the case in our simulations. Assuming that the shape of the interface is linear, the analytical model of Tanino *et al.* (2005) predicts $\alpha = 0.67$ for currents with a high volume of release. However, as the shape of the interface is not linear in our simulation, the comparison with the model of Tanino *et al.* (2005) is not appropriate. We mention in passing that unpublished simulations conducted in our group of lock-exchange currents, with a small volume of release propagating over a rough bed, predicted the presence of a drag-dominated regime past the buoyancy–inertia phase in which, as expected, $U_f \sim t^{-1/3}$. During the drag-dominated regime, the simulations

predicted $U_f \sim t^{-1/2}$, which agrees with the analytical model of Hatcher *et al.* (2000) for the case of high-Reynolds-number currents forming due to a finite instantaneous release of lock fluid.

4. Structure of the gravity current

4.1. Interaction between the head and the obstacles

The changes in the structure of the head and the dissipative wake regions as the front propagates over the fourth rib are illustrated in figure 4(b–e) by means of the concentration fields for the simulations in which the gravity current reaches a slumping phase as it propagates over the obstacles. Several mechanisms are responsible for the significant decay of the concentration in the head region in the simulation with ribs with respect to the flat-bed case (e.g. compare figures 4a and 4b when x_f is close to $14H$). These mechanisms are related to the changes in the flow structure behind the front induced by the interaction between the head and the obstacles.

The height of the head before the current starts interacting with the ribs (figure 4b) is about 2.5 times that of the obstacle. As the front impacts the upstream face of a rib (figure 4c), the head is projected upwards and a backward-propagating hydraulic jump forms. The position of the jump is visualized in figure 4(c–e). The maximum height reached by the splashed fluid is about 4 times the height of the obstacle. The sudden change in the flow direction as a result of the impact creates strong turbulent eddies. This is the first important mechanism that increases the mixing with the surrounding lower-density ambient fluid at the front of the current. The fluid inside the splash loses most of its streamwise momentum and, after it is convected over the top of the rib, starts plunging downwards, at a low angle with the vertical. Part of this plunging fluid is diverted in the upstream direction. As the heavier fluid originating in the initial splash reattaches to the bed (figure 4d), a patch of low-density ambient fluid is trapped in between the downstream face of the rib and the higher-density fluid moving towards the bed surface. The trapped lower-density fluid is pushed upwards by the plunging fluid moving in the upstream direction and starts mixing with it (figure 4d). This is the second important mechanism that increases mixing and reduces the mean concentration of the fluid in the head region. Both mechanisms are similar to those observed for isolated ribs (e.g. see Gonzalez-Juez *et al.* 2009).

The heavier fluid convected over the obstacle changes direction gradually and orients itself parallel to the flat part of the bed surface. During this time, a region of highly accelerated and relatively high-density fluid (figure 4e) develops past the downstream face of the rib. For the conditions considered in case LR-R15, the flow in this region becomes supercritical for all the five ribs. This region, which we refer to as the jet-like flow, has the form of a wall-attached jet after the current attaches to the bed surface. The angle of the jet-like flow with the vertical diminishes gradually as the jet-like flow strengthens and the size of the recirculation region downstream of the rib increases. A hydraulic jump forms as the flow transitions from supercritical in the upstream part of the jet-like flow to subcritical in the head region. Besides increasing the mixing at the back of the head (figure 4e), the interaction of the jet-like flow with the back of the head induces the formation of a strong intensified mixing vortex (IMV). Such vortices were observed experimentally by Alexander & Morris (1994) in the flow past an isolated ridge. These vortices are very dissipative due to the small-scale turbulence induced by the hydraulic jump and entrained into their cores.

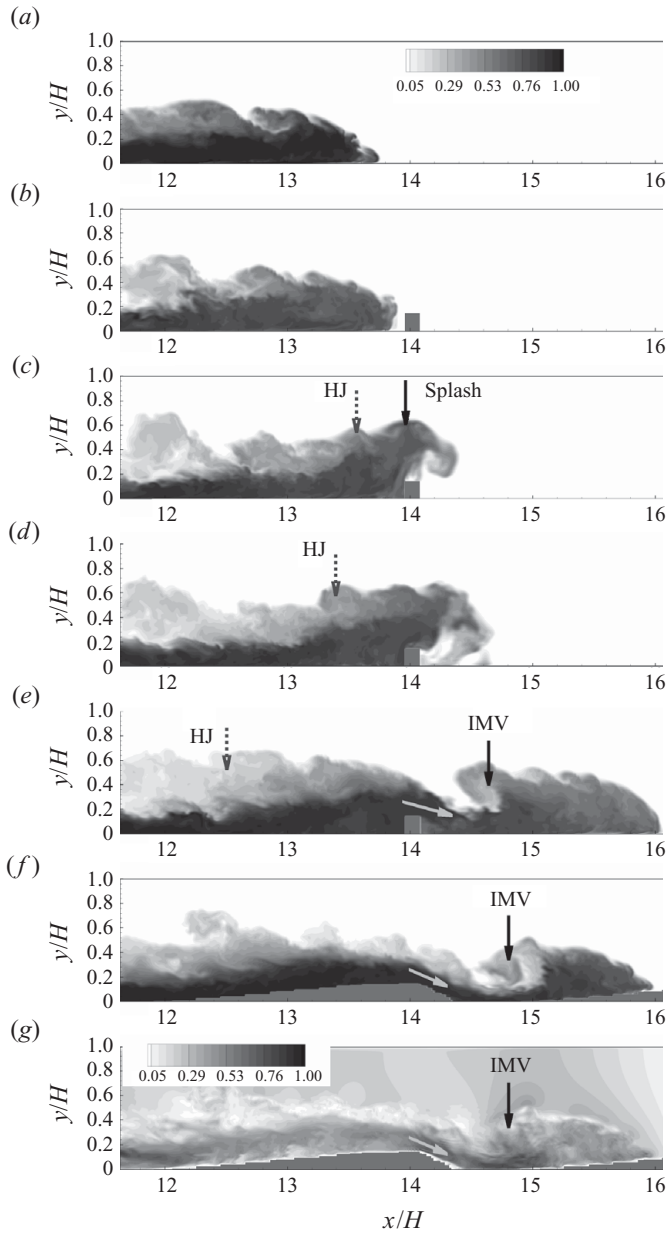


FIGURE 4. Visualization of the temporal changes in the concentration field in a $z = \text{constant}$ plane as the gravity current overtakes the fourth rib in the LR-R15 simulation ($b-e$). Frame (a) shows the concentration field in the flat-bed (LR-F) simulation when the front is close to $x/H = 14$. Also shown in (f and g) are the distributions of the concentration and velocity magnitude in the LR-D15 simulation, when the front is situated at the same position as in (e). Frames ($b-e$) show the formation of the initial splash of the denser fluid as the front reaches the upstream face of the rib, of the high-velocity jet-like flow and the intensified mixing vortex after the front passes the obstacle. The grey arrows in ($e-g$) show the direction of the jet-like flow. The dashed-line arrows in ($c-e$) show the position of the backward-propagating hydraulic jump (HJ) originating at the fourth rib. Frame (g) visualizes the jet-like flow region in the simulation with dunes.

The axis of the IMV is initially situated at about $0.5H$ from the rib (figure 4e). The vortex is pushed slowly away from the rib that induced its formation (from $0.5H$ to about $1.0H$) until the front reaches the next rib. Thereafter, the position of the vortex does not change in time.

The dynamics of the flow in the head region in the simulation with dunes has many qualitative similarities with those observed in case LR-R15. As can be seen from the comparison of the concentration distributions in figures 4(e) and 4(f), the presence of the jet-like flow (the velocity amplification within the jet-like flow is visualized figure 4g for case LR-D15) and the formation of the IMV are common features of both cases. The main difference is the absence of the splash of higher-density fluid during the time the front propagates over the upslope face of the dune. A second reason for the fact that the mixing at the head of the current is weaker in the simulation with dunes is that the flow remains attached after the front overtakes the crest of the dune. Still, as the nose plunges downwards, lower-density fluid situated in the vicinity of the lee face is trapped beneath the nose and mixes with the higher-density fluid inside the head.

The physics of the interaction between the head of the current and the obstacles does not change much in case LR-R15-HD during the propagation of the current in the drag-dominated regime, and hence we do not show an additional figure. Even though the ribs are much more closely spaced, the distance between them is sufficient for the heavier fluid to reattach well in front of the next rib and for the front to recover its usual shape before it starts interacting with the next rib in the series. The main difference is that the flow does not become supercritical within the jet-like flow even for the ribs situated immediately behind the front (see also discussion of figure 7).

4.2. Tail structure

The structure of the tail in the low-Reynolds-number simulations with a flat bed and with obstacles ($D = 0.15H$, $\lambda = 3H$) is compared in figure 5 at the time when $x_f \cong 19H$ in all the three simulations. Closely related with this, figure 6 compares the streamwise distributions of the local height and Froude number of the current. Consistent with the findings of Shin *et al.* (2004), Necker *et al.* (2005) and Cantero *et al.* (2007), we estimate the height \bar{h} and mean streamwise velocity \bar{u} used to calculate the Froude number ($Fr = \bar{u}/\sqrt{\bar{h}}$) at a certain streamwise location inside the gravity current as $\bar{h} = (1/H) \int_0^H C \, dy$ and $\bar{u} = (1/u_b) \int_0^H uC \, dy / \int_0^H C \, dy$.

Consistent with the findings of Ooi *et al.* (2009) for strongly turbulent currents ($Re_f > 10^4$) with $R = h/x_0 \ll 1$, the concentration distribution in figure 5(a) shows that in the flat-bed case a stably stratified diffuse interface, depleted of large-scale eddies, develops between the heavier current and the lighter ambient fluid, starting at the position of the lock gate. In the later stages of the slumping phase ($x_f/H > 10$), this diffuse interface ends at about $5H$ behind the front. The KH billows forming at the back of the head lose their coherence over a distance of about $4.5H$. The stably stratified interface is slightly tilted with respect to the horizontal. The height of the dense fluid layer reaches a minimum at the end of the interface region. It remains fairly constant in the dissipative wake region, before increasing again in the head region. As shown in figure 5(c), the streamwise velocity inside the heavier current peaks at the end of the tilted interface and over the upstream part of the dissipative wake region where $u \cong 0.7u_b$. The velocity decreases gradually as the front region, where $U_f \cong 0.45u_b$, is approached. The velocity magnitude is close to zero within

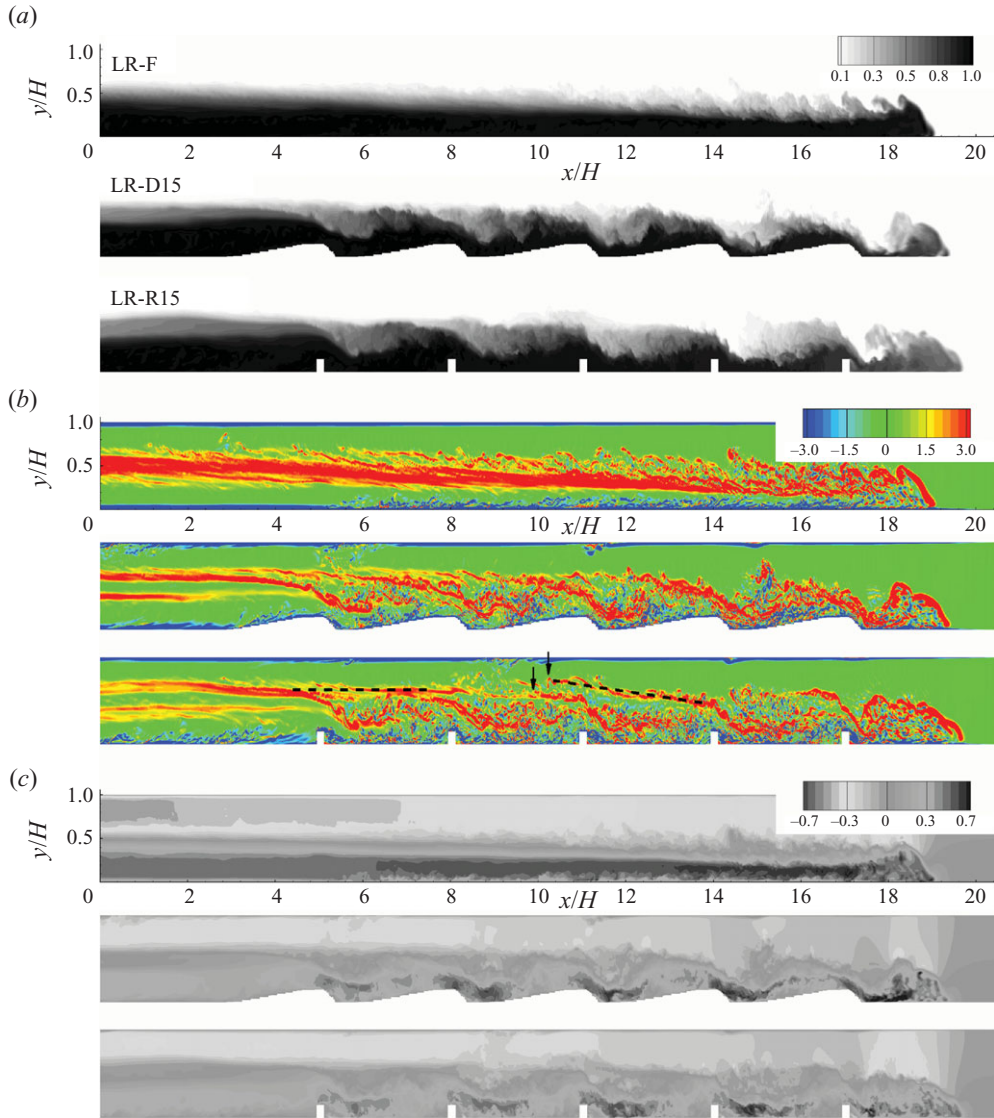


FIGURE 5. (Colour online) Visualization of the structure of the lock-exchange flow in a $z = \text{constant}$ plane in the LR simulations with a flat bed and with obstacles ($D = 0.15H$, $\lambda = 3H$) at the time when $x_f/H \cong 19$. (a) Concentration, C ; (b) out-of-plane vorticity, $\omega_z H / u_b$; (c) streamwise velocity, u / u_b . The figures show the formation of a strong jet-like flow region past the crest/top of the obstacles within the bottom-propagating current and allow comparison of the shapes of the layers of lighter (ambient), mixed and denser fluid over the tail of the current. Note that the vertical axis has been stretched by a factor of two in all frames. The dashed lines in (b) show the upstream parts of the shear layers induced by the formation of the jet-like flow at rib 2, in the region between rib 1 and rib 2, and at rib 4, in the region between rib 3 and rib 4. The two arrows in (b) show that two distinct shear layers are present over rib 3.

the tilted interface layer containing mixed fluid. The thickness of the region of small velocity magnitude increases slightly in the dissipative wake region due to the presence of large-scale interfacial billows.

The structure of the current is very different when dunes or ribs are present. A layer of varying height containing mixed fluid develops between the regions containing heavier ($C > 0.9$) fluid and light ambient fluid ($C = 0$). The top of this layer is close to horizontal in the LR-R15 and LR-D15 simulations. The bottom of this layer undergoes quasi-regular deformations with the same wavelength at that of the obstacles ($\lambda = 3H$). The velocity inside this layer is very small. The regions of high velocity in figure 5(c) correspond to the jet-like flow discussed above. Once they form, the jet-like flow and the shear layer on its outer side (towards the ambient fluid) are permanent features of the flow around the obstacles. The distributions of the spanwise vorticity in figure 5(b) show that the downstream extent of the shear layer past the crest or downstream face of the obstacle is larger in case LR-R15 ($2.25H$) compared with case LR-D15 ($1.5H$). The main temporal change in the region associated with the jet-like flow is that, after the front gets sufficiently far from the obstacle, the flow remains subcritical. In the present simulations, this happens starting with the second or third obstacle behind the front.

Next, the effects of the temporal evolution of the backward-propagating jumps (e.g. see figure 4d,e) on the structure of the tail region are discussed (see also supplementary movie 1 available at journals.cambridge.org/flm). Some of these effects can be inferred from analysing the structural changes of the flow between consecutive obstacles with increasing distance between the obstacles and the front, at a given time instance (see figure 5). The formation of the backward-propagating hydraulic jump amplifies the strength of the upstream part of the shear layer on the upper side of the jet-like flow. As the jump propagates, the shear layer extends further upstream and becomes more horizontal (e.g. compare the position of the shear layer in between the first two obstacles and in between the third and fourth obstacles in figure 5b). As the hydraulic jump reaches the obstacle situated behind the one where it originated, and propagates over this obstacle, the shear layer continues to expand upstream. At those locations (e.g. around rib 3 in figure 5b), two shear layers containing vorticity of the same (positive) sign can be observed. As time passes, these shear layers merge and the interface between the layer of mixed fluid and the top layer of ambient fluid becomes close to horizontal (e.g. similar to that observed in between the first two obstacles in figure 5b). Thus, the structure of the layer of variable height containing low-velocity mixed fluid (see figures 5a and 5c) is determined by the interactions of the backward-propagating hydraulic jumps with the obstacles situated upstream of the one at which the jumps originated and with the jet-like flow over these obstacles.

A strong shear layer containing vorticity of opposite (negative) sign to that in the shear layer on the upper side of the jet-like flow is present at the boundary between the jet-like flow and the recirculation region forming past the rib. This region is not present in the simulation with dunes, for which the flow past the crest of the dunes remains for the most part attached. However, because the core of high-velocity fluid within the jet-like flow is slightly diverted away from the dune surface past the dune trough, a near-bed region of small velocity magnitude is present at about the middle of the leeside of each dune (e.g. around $x/H = 10, 13$ and 16 in figure 5). The flow does not separate but a strongly dissipative shear layer forms (see discussion of figure 12c).

A comparison of the streamwise distributions of \bar{h} and Fr in cases LR-F and LR-R15 (figure 6) allows characterizing in an integral sense the differences in the structure of a gravity current propagating over a flat bed and over a bed with surface-mounted ribs. In the flat-bed case, the height of the current decays linearly from the

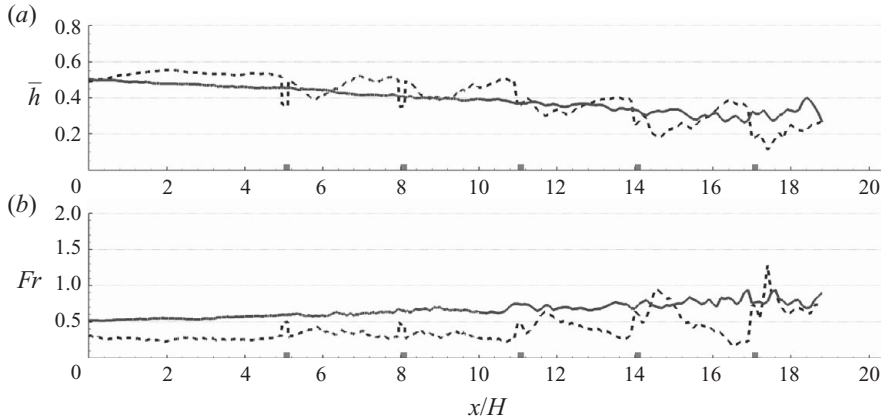


FIGURE 6. Streamwise variation of (a) height of the gravity current, \bar{h} , and (b) Froude number, Fr , in the LR-F (solid line) and LR-R15 (dashed line) simulations at the time when $x_f/H \cong 19$.

position of the lock gate where $\bar{h} = 0.5$ (the flow is effectively antisymmetric with respect to $x/H = 0$) until the end of the region where the stratified interfacial tilted layer is present (e.g. $x \cong 15H$ when $x_f/H = 18.8$). It then remains approximately constant until the head region ($17H < x < 18.8H$) is reached. The presence of a raised head explains the increase of \bar{h} around $x = 18.2H$. The increase of Fr with the streamwise distance in the region where the tilted interface is present ($x < 15H$) can also be considered linear, to a good approximation. The Froude number remains fairly constant ($Fr \cong 0.8$ for $15H < x < 18.8H$) until close to the nose of the current. As expected, the values of the Froude number remain less than 1 over the whole length of the current propagating over the flat horizontal surface. For the flow to become supercritical, a sloped flat surface with a sufficiently high negative slope is required.

In case LR-R15, the variations of \bar{h} and Fr in between the first and second ribs and in between the second and third ribs are close to identical (figure 6). This means that when $x_f/H = 18.8$, the flow has reached a quasi-steady state up to the position of the third rib. The average value of \bar{h} in the quasi-steady state region is close to $0.5H$, while that of Fr is close to 0.35. The mean level of \bar{h} in between two consecutive ribs starts decaying as the front is approached (e.g. past the third rib in figure 6). This is caused by the high level of mixing induced over the downstream part of the current by the interaction between the head of the current and the obstacles. The variation of Fr with x in this region is opposite to that of \bar{h} . The Froude number peaks at a distance of approximately $0.5H$ from the ribs in the downstream part of the current. The peak value of Fr in between two consecutive ribs decreases with the distance between the ribs and the front. In particular, for the set-up considered in case LR-R15, the flow behind the most recent rib overtaken by the front becomes supercritical ($Fr = 1.2$) in the region where the jet-like flow reaches the horizontal bed surface. This is consistent with the analytical model of Armi (1986) for isolated bottom-mounted obstacles with slowly varying height and the shallow-water analysis of Gonzalez-Juez & Meiburg (2009), who found that the flow can be supercritical immediately downstream of the crest/top of a single obstacle, but transitions to subcritical further downstream. In the present case of a periodic array of ribs, by the time the front passes the next rib, the jet-like flow is already subcritical.

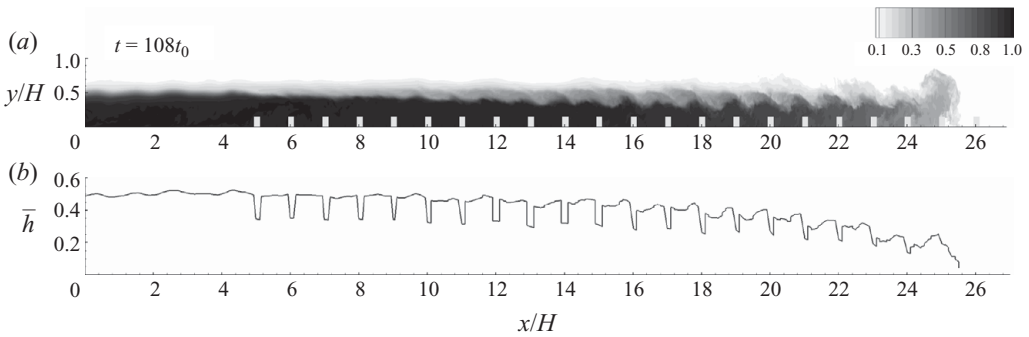


FIGURE 7. Visualization of the structure of the lock exchange flow in the LR-R15-HD simulation at $t = 108t_0$, when $x_f/H \sim 25.5$. (a) Concentration, C ; (b) height of the gravity current, \bar{h} . Note that the vertical axis has been stretched by a factor of two in (a).

The overall trends in the variations of \bar{h} and Fr are similar in the simulations with ribs and dunes (not shown). The main difference is that the peak values of Fr in between two consecutive obstacles situated in the downstream part of the current are larger in the simulation with dunes. For example, the peak values of Fr downstream of the fourth and fifth dunes are 1.1 and 2.2, respectively. The corresponding values of Fr are 0.9 and 1.2 in the simulation with ribs (figure 6). In case LR-D15, the peak values of Fr are reached immediately downstream of the location of the crest of the dunes and are primarily due to the strong decay of \bar{h} over the upslope face of the dunes. An analysis of the distributions of the same variables over the tail of the current in the simulations conducted at $Re = 10^6$ shows that scale effects are insignificant for $47800 < Re < 10^6$.

Figure 7(a) shows the structure of the current in the LR-R15-HD simulation at $t = 108t_0$, after the front has overtaken the 21st ($x_f/H \cong 25.5$) rib in the series. At this time instant, the current is well into the drag-dominated regime. The concentration distribution in figure 7(a) is qualitatively similar to that predicted in case LR-R15 when $x_f/H \cong 19$ (figure 5a). For example, the interface between the layer of mixed fluid and the layer of ambient fluid is very close to horizontal between the lock gate and $x/H = 10$. For the same position of the front, the average value of the concentration in the head region is smaller in the LR-R15-HD simulation compared with the LR-R15 simulation (e.g. when $x_f/H \cong 19$, $C \cong 0.55$ in the LR-R15 simulation and $C \cong 0.45$ in the LR-R15-HD simulation). This is because of the larger number of obstacles per unit streamwise length which increases mixing compared with case LR-R15. The distance between the front and the region containing fluid with a concentration ($C > 0.9$) close to that of the lock fluid increases monotonically with time (e.g. from about $7H$ at $t = 77t_0$ to $10H$ at $t = 108t_0$).

Similar to case LR-R15 (figure 6), the mean value of \bar{h} in between two consecutive ribs is close to constant over the upstream part of the current ($x/H < 14$ in figure 7b). With the exception of the regions situated on top of the ribs, the values of \bar{h} are close to $0.5H$. A comparison of the distributions of the velocity magnitude at different times during the drag-dominated regime shows that the velocity field decays relatively uniform with time over the whole length of the bottom-propagating current. This means that the mean value of Fr in the upstream part of the tail will decay with time, rather than being constant as in case LR-R15. The downstream part of the current (e.g. $x/H > 14$ at $t = 108t_0$) is characterized by a nonlinear increase of the average

value of \bar{h} in between two consecutive ribs with the distance between the front and the ribs. During the drag-dominated regime, the flow remains subcritical over the whole length of the current in the LR-R15-HD simulation. For example, at $t = 108t_0$ the maximum value of Fr is smaller than 0.5 everywhere, including over the top of the rib situated immediately behind the front.

5. Energy budget

Following the approaches used by Necker *et al.* (2005) and Ooi *et al.* (2009), in the case of compositional gravity currents a differential equation relating the rates of change of the potential and kinetic energy can be obtained if the velocity components are assumed to be equal to zero on all the non-periodic boundaries and the effects of diffusion in the transport equation solved for the concentration field are neglected:

$$\frac{dE_k}{dt} = -\varepsilon - \int_{\Omega} C u_2 dV = -\varepsilon - \frac{dE_p}{dt}, \tag{5.1}$$

where $E_k = \int_{\Omega} 0.5u_i u_i dV$ is the total kinetic energy over the flow domain $\Omega = L_1 L_2 L_3$, $E_p = \int_{\Omega} C x_2 dV$ is the total potential energy, and ε is the total dissipation rate. Its expression is

$$\begin{aligned} \varepsilon &= \int_{\Omega} \varepsilon_r(x_1, x_2, x_3, t) dV \\ &= \int_{\Omega} \varepsilon_r dV = \int_{\Omega} u_i \frac{\partial}{\partial x_k} \left[\left(\frac{1}{Re} + \nu_{SGS} \right) \left(\frac{\partial u_i}{\partial x_k} + \frac{\partial u_k}{\partial x_i} \right) \right] dV, \end{aligned} \tag{5.2}$$

where ε_r is the local dissipation rate. An integral balance equation for the mechanical energy can be obtained by integrating (5.1) with time:

$$E_k + E_p + E_d = E_{k0} + E_{p0}, \tag{5.3}$$

where E_{k0} and E_{p0} are the total initial kinetic energy and potential energy. As the present simulations are started from rest, $E_{k0} = 0$. The term $E_d = \int_0^t \varepsilon(\tau) d\tau$ is the time integral of the total dissipation rate.

The variation of the terms in (5.3) with the front position is plotted in figure 8(a) for the simulations conducted at $Re = 47\,800$ with flat bed and with obstacles ($D = 0.15H$, $\lambda = 3H$). Figure 9 shows the effect of increasing the Reynolds number on the energy budget in the simulations with a flat bed and with ribs. All the terms are non-dimensionalized by E_{p0} .

A first regime characterized by the conversion of potential energy into kinetic energy is present at the start of all the simulations. This regime corresponds approximately to the duration of the acceleration phase ($t < 3.5t_0$). The process is essentially inviscid, as not much dissipation takes place during this regime ($E_d(t = 3.5t_0)/E_{p0} \cong 0$).

In the LR-F simulation, the growth of E_k and E_d with time is linear for $t > 18t_0$. This can be inferred from the log–log plot in figure 8(b), where the variations of these two variables can be approximated by a straight line with a slope of 1 and from the plots of dE_k/dt and ε in figure 10. Figure 10 shows that the linear regime is observed until the end of the simulation ($t \cong 40t_0$). During the linear regime, the ratio of ε to $-dE_p/dt$ is 0.32 and that of dE_k/dt to $-dE_p/dt$ is 0.68. The time variations of E_k , E_p and E_d are qualitatively similar in the two simulations with a flat bed. As Re increases from 47 800 to 10^6 , the temporal rate of growth of E_k during the linear regime increases from $0.07u_b^3 h^2$ to $0.085u_b^3 h^2$ (figure 9a). This increase is mainly due

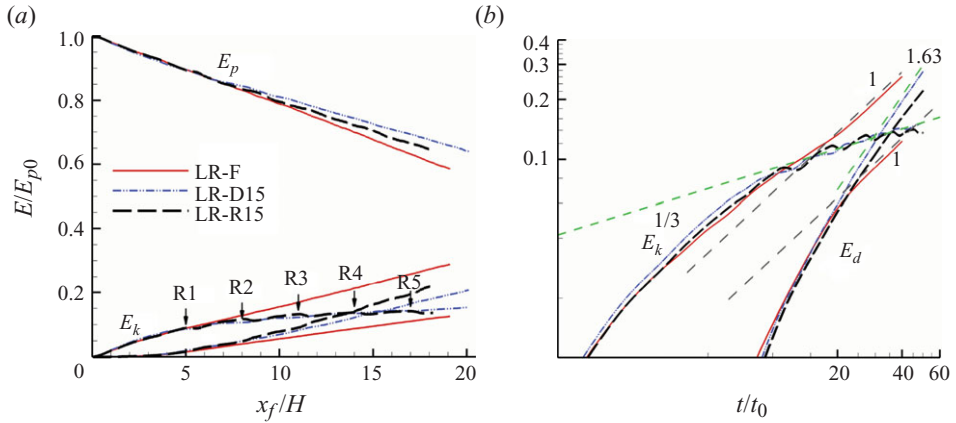


FIGURE 8. (Colour online) Variation of the potential energy, E_p , kinetic energy, E_k , and integral of the total dissipation, E_d , in the LR simulations with a flat bed and with obstacles ($D=0.15H$, $\lambda=3H$). In (a) plotted versus the front position in linear–linear scale; (b) plotted versus time in log–log scale. All the terms are non-dimensionalized by the initial potential energy E_{p0} . The arrows in (a) indicate the position of the ribs in the LR-R15 simulation. The dashed lines in (b) indicate a best fit of the form γt^α (γ is a constant) for E_k and E_d . The values of α are given in the plot. The figure shows that in the simulations with obstacles, the current reaches a regime where $E_k \sim t^{1/3}$, while in the flat-bed simulation the current reaches a regime where $E_k \sim t$.

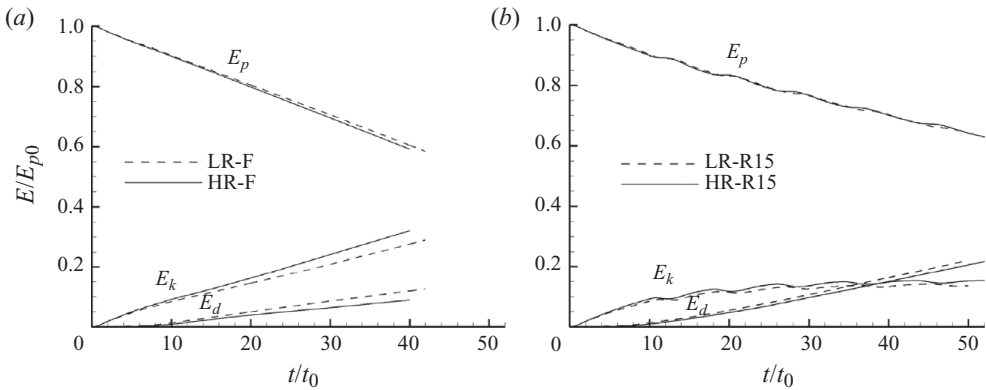


FIGURE 9. Effect of the Reynolds number on the time variation of the potential energy, E_p , kinetic energy, E_k , and integral of the total dissipation, E_d . (a) Simulations with a flat bed; (b) simulations with ribs. All the terms are non-dimensionalized by the initial potential energy E_{p0} .

to a reduction of ε from $0.035u_b^3h^2$ to $0.022u_b^3h^2$. During the linear regime, the ratio of ε to $-dE_p/dt$ is 0.22 and that of dE_k/dt to $-dE_p/dt$ is 0.73 in the HR-F simulation. The increase in the Reynolds number causes a reduction in ε over the linear regime of about 33 %.

As will be analysed below in greater detail, the combined effect of the smaller decay rate of E_p and higher dissipation rate within the body of the gravity current observed in the simulations with obstacles causes a smaller increase of E_k with x_f for $x > 5H$

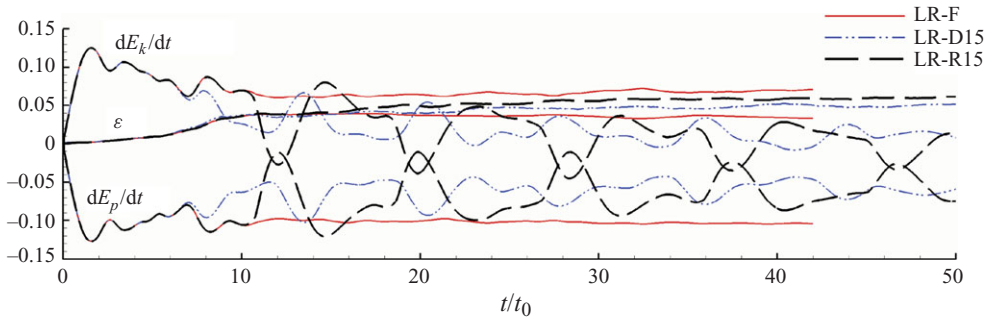


FIGURE 10. (Colour online) Time variation of the terms (dE_k/dt , dE_p/dt and ε) in the differential equation of the mechanical energy in the LR simulations with a flat bed and with obstacles ($D=0.15H$, $\lambda=3H$). All the terms are non-dimensionalized by $u_b^3 H^2$.

compared with the flat-bed case. This partially explains the observed decrease of the front velocity in the simulations with obstacles compared with that with a flat bed.

The most important qualitative change with respect to the flat-bed case is observed in the variation of E_k . After the current passes the first obstacle, the rate of increase of E_k is reduced substantially and, after it overtakes the second obstacle ($x_f > 9H$), a regime in which E_k increases proportionally to $t^{1/3}$ ($dE_k/dt \sim t^{-2/3}$) is maintained until the end of the simulation for both types of obstacles (see figures 8*b* and 10). The large-scale oscillations in the variation of E_k and dE_k/dt in figures 8(*b*) and 10 are induced by the successive acceleration and deceleration of the flow in the head of the current due to its interaction with the obstacles. The fact that the temporal variations of dE_k/dt and dE_p/dt are out of phase and that such oscillations are absent in the variation of ε in figure 10 shows that the large-scale oscillations in the variation of dE_k/dt are a direct consequence of the vertical movement of the heavier fluid within the head of the current as it propagates over the deformed bed surface.

The rate of decay of E_p is smaller than that computed for the flat-bed case after the front passes the first obstacle. When plotted versus the front position, the smallest rate of decay is observed in the simulation with dunes (figure 8*a*). A short time after the front overtakes the second obstacle, the curves showing the variation of E_d with x_f start diverging. The increase of E_d with time in the simulations with obstacles is faster ($\sim t^{1.63}$) than the linear increase observed in the simulation with a flat bed. For $x_f > 9H$, figure 8(*a*) shows that E_d increases faster with x_f in the simulation with ribs, as compared with the simulation with dunes. This is because the presence of the ribs increases dissipation, especially within the shear layers forming on the two sides of the jet-like flow, compared with the case of obstacles with a lower degree of bluntness (dunes). Meanwhile, the variation of E_k with x_f remains independent of the shape of the obstacle for $x_f > 9H$.

In contrast to the results for the flat-bed case, when obstacles are present at the channel bottom, the temporal evolution of the terms in the energy budget is very similar not only qualitatively but also quantitatively in the simulations conducted at $Re=47\,800$ and $Re=10^6$. For example, the comparison of the energy budgets in the LR-R15 and HR-R15 simulations (figure 9*b*) shows that the increase of E_d with time is slightly slower in case HR-R15, while the decay of E_p with time is independent of the Reynolds number. This is consistent with the slightly larger front velocity predicted in case HR-R15 ($U_f=0.36u_b$) compared with case LR-R15 ($U_f=0.34u_b$).

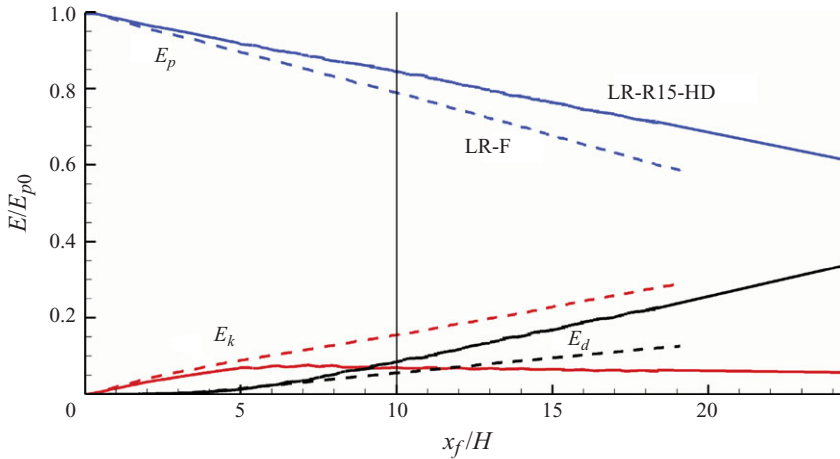


FIGURE 11. (Colour online) Variation of the potential energy, E_p , kinetic energy, E_k , and integral of the total dissipation, E_d , with the front position in the LR-R15-HD simulation. All the terms are non-dimensionalized by the initial potential energy E_{p0} . The vertical line marks the start of the regime where the variation of the three quantities with x_f is linear.

Scale effects on the energy budget are even less significant in the simulations with dunes for which the front velocity is the same ($U_f = 0.4u_b$).

Figure 11 shows the variations of E_k , E_p and E_d with x_f in the LR-R15-HD simulation with densely spaced ribs. Compared with case LR-R15 (figure 8a), the variation of E_p in case LR-R15-HD is qualitatively similar. After the current overtakes the first couple of ribs in the series ($x_f/H > 10$), the decay of E_p with x_f is close to linear and has a constant slope until the end of the simulation. The decay rate of E_p is significantly smaller than that observed in the flat-bed case. Also, at about the same front position ($x_f/H = 10$), the increase of E_d with x_f becomes close to linear. The rate of increase of E_d is significantly higher compared with the flat-bed case due to the additional dissipation generated by the interaction of the current with the ribs situated behind the front.

The most important difference in the energy budgets for cases LR-R15 and LR-R15-HD is observed for E_k . The current reaches the slumping phase around $t = 22t_0$ ($x_f/H > 9$) for case LR-R15. Its front velocity remains approximately constant until the end of the simulation ($t/t_0 \cong 50$). As time passes, a larger volume of fluid is set into motion. As the front velocity is constant, E_k should continue to increase with time. Indeed, the results in figure 8(b) show that $E_k \sim t^{1/3}$. This increase is smaller than that observed in the flat-bed case where $E_k \sim t$. In contrast to these two simulations in which the current does not leave the slumping phase, E_k starts decaying with time for case LR-R15-HD during the transition to the drag-dominated regime ($x_f/H \sim 7$).

To a good approximation, the decay of E_k with both x_f and time for $t > 22t_0$ is close to linear until the end of the simulation ($t \cong 110t_0$). The decay of E_k with time is consistent with the fact that the front velocity does not reach a regime where U_f is constant during the later stages of its propagation (figure 3a), corresponding to a slumping phase of the current propagating over the ribs. For that to happen, E_k should start increasing with time. The trends observed in figure 11 for the three terms of the energy budget do not suggest this will be the case. The results in figures 3 and 11 show that a drag-dominated regime characterized by the decay of the front

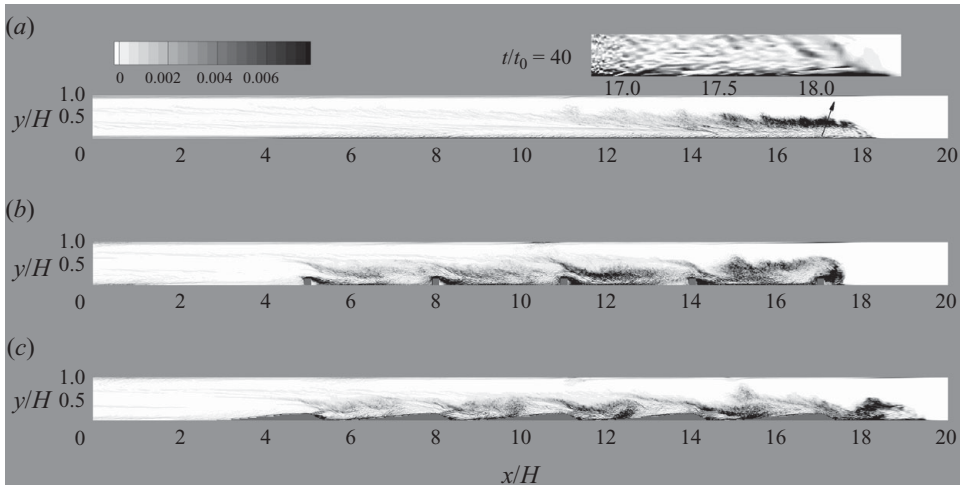


FIGURE 12. Spatial distributions of the non-dimensional spanwise-averaged local dissipation rate $\tilde{\epsilon}/(u_b^3/H)$. (a) LR-F ($t/t_0 = 40$), (b) LR-R15 ($t/t_0 = 48$) and (c) LR-D15 ($t/t_0 = 48$). The figure shows that while in the flat-bed case most of the dissipation occurs in the head and dissipative wake regions, in the simulations with obstacles, most of the dissipation occurs in the tail of the current. The inset in (a) visualizes the thin bottom layer of high $\tilde{\epsilon}$ in case LR-F.

velocity and total kinetic energy with time and the front position is present in case LR-R15-HD. The distributions of the dissipation rate discussed in the next section will provide more detailed information on how the presence of the obstacles modifies the flow structure and increases the total dissipation over the tail region with respect to the flat-bed case.

6. Dissipation rate

An analysis of the distribution of the spanwise-averaged local dissipation rate $\tilde{\epsilon}(x_1, x_2, t)$ allows to better understand the changes in the structure of a gravity current as a result of the presence of the obstacles at the bed. To study the distribution of the dissipative losses along the channel, the local dissipation rate ϵ_r is integrated over the spanwise and vertical directions. This leads to a new variable $\epsilon^{23}(x_1, t) = \int^{L_3} \int^{L_2} \epsilon_r(x_1, x_2, x_3, t) dx_3 dx_2$.

6.1. Effects due to the presence of obstacles

After the head passes the first rib, the distributions of $\tilde{\epsilon}$ in the three simulations start showing important qualitative and quantitative differences. Figure 12 shows $\tilde{\epsilon}$ during the later stages of the slumping phase, when the front is situated between $17H$ and $20H$ in the three simulations.

Beyond the initial stages ($t/t_0 > 15$) of the slumping phase, most of the dissipation in case LR-F (e.g. see figure 12a) takes place in the thin bottom boundary layer and in the billows present in the interfacial region. Consistent with the results of Bonometti *et al.* (2008) obtained for lower-Reynolds-number Boussinesq currents, the dissipation inside the bottom boundary layer is smaller but comparable with that inside the interfacial region. For example, at $t = 40t_0$, the bottom boundary layer

accounts for 40 % of the total dissipation, while the interfacial region accounts for 60 %.

In the LR-R15 simulation (figure 12*b*), the regions of strong dissipation correspond to the shear layers forming in between the jet-like flow and the separated region downstream of the rib and to the shear layers on the upper side of the jet-like flow. The dissipation levels are also relatively high in the core of the intensified mixing vortex situated closest to the front. As the head propagates away from the vortex, the dissipation inside its core decreases quite fast.

Compared with the flat-bed case, the dissipation level inside the interfacial billows shed behind the head is smaller. In the simulations with obstacles, the length of the interfacial region behind the head in which the local dissipation rate is relatively high ($\tilde{\varepsilon} > 0.005u_b^3/h$) decreases with time (e.g. its length is about H at $t/t_0 = 16$ and $0.5H$ at $t/t_0 = 32$). Similar to case LR-R15 (figure 12*b*), the distributions of $\tilde{\varepsilon}$ in case LR-D15 (figure 12*c*) show that in the later stages of the propagation of the current ($t > 20t_0$), most of the dissipation takes place behind the dissipative wake. However, because the dense fluid layer does not separate as it is convected past the crest of each dune (this is different from the case of a constant density flow over the same dunes), there is no shear layer in between the core of high-velocity and high-density fluid and the bed. Thus, immediately past the crest of the dune, most of the dissipation takes place in the shear layer forming on the upper side of the jet-like flow. Compared with case LR-R15, the average levels of $\tilde{\varepsilon}$ inside this shear layer are lower. The upstream propagation of the heavier fluid with the successive hydraulic jumps forming at the crest of the obstacles strengthens the vorticity and dissipation inside this shear layer. The hydraulic jumps are sharper in the case of bluff-body obstacles like ribs.

The presence of dunes induces another qualitative modification in the flow structure past the crest of the dune. Before dissipating, the IMV is strong enough to induce a change in the orientation of the core of high-speed fluid within the jet-like flow. The core is diverted slightly away from the bed in the region situated beneath this vortex. This explains the presence of a region of high dissipation close to the bed, starting a short distance from the trough of the first couple of dunes situated behind the front (e.g. around $x = 12.5H$ and $x = 15.5$ in figure 12*c*).

The distribution of ε^{23} is plotted in figure 13 at several non-dimensional times which are representative of the evolution of the current past the initial stages of the slumping phase in cases LR-F, LR-R15 and LR-D15. The total dissipation in between two successive ribs decreases with the distance between the front and these ribs. For example, at $t = 48t_0$ the ratios between the total dissipation in these regions, starting with that situated the closest to the front, and the total dissipation in the region with $x/H > 0$ are 31 %, 24 %, 20 % and 13 %, respectively. At the same time, the head and dissipative wake regions account for only 9 % of the total dissipation in the region with $x/H > 0$ in case LR-R15. The total dissipation in the head and dissipative wake regions is about three times lower than the total dissipation in between the first two ribs situated behind the front. In contrast, in the flat-bed case, the total dissipation in the head and dissipative wake at $t = 40t_0$ is more than two times larger than that in the tail. A comparison of the distributions of ε^{23} in the simulation with dunes ($t = 40t_0$) and ribs ($t = 48t_0$) shows that, for a given front position, the total dissipation in the region between two successive dunes or ribs situated at the same distance from the front is comparable. The average levels are slightly higher in the simulation with ribs, consistent with the fact that the magnitude of the total dissipation rate is slightly higher for ribs when ε is plotted as a function of the front position.

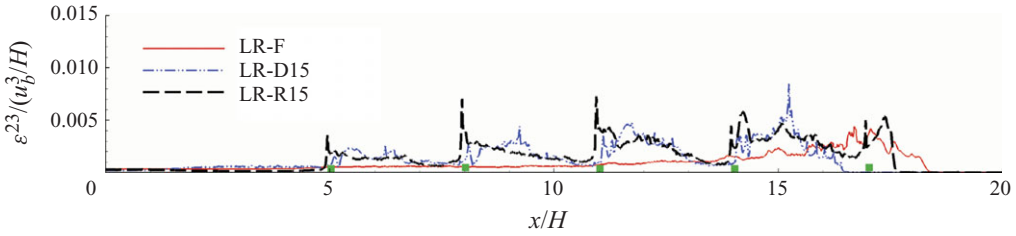


FIGURE 13. (Colour online) Streamwise distributions of $\varepsilon^{23}(x_1)/(u_b^3 H)$ in the LR-F ($t/t_0 = 40$), LR-R15 ($t/t_0 = 48$) and LR-D15 ($t/t_0 = 40$) simulations.

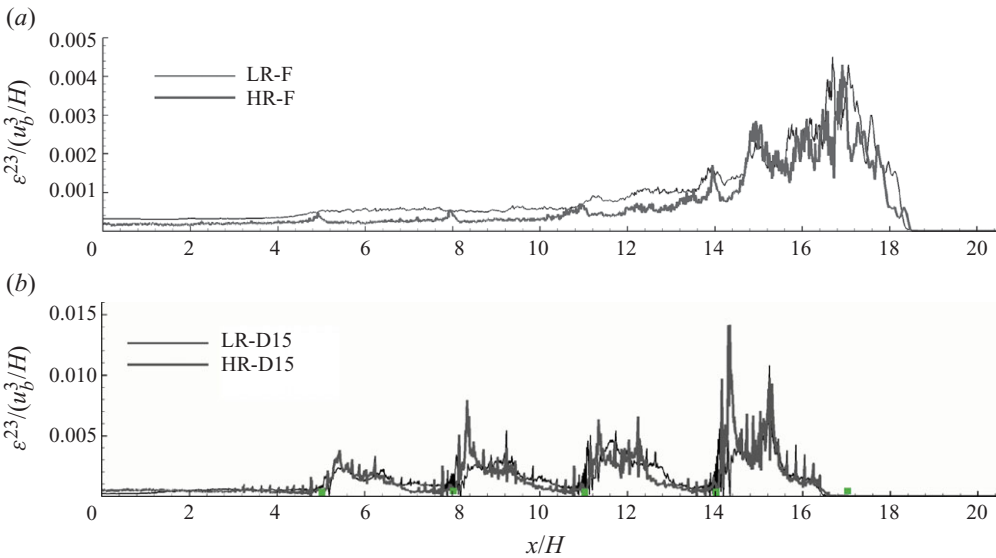


FIGURE 14. (Colour online) Effect of the Reynolds number on the streamwise distributions of $\varepsilon^{23}(x_1)/(u_b^3 H)$. (a) Simulations with a flat bed, $t/t_0 = 40$ (LR-F) and $t/t_0 = 38$ (HR-F), and (b) simulations with dunes, $t/t_0 = 40$ (LR-D15 and HR-D15). The square ribs indicate the position of the crest of the dunes.

6.2. Scale effects

The effect of the Reynolds number is discussed next, based on the comparison of the distributions of ε^{23} in the simulations conducted at $Re = 47\,800$ and $Re = 10^6$. In the case of a flat bed, the main effect of increasing Re is the decay of the dissipation in the tail region (figure 14a). Most of the dissipation in the tail takes place in the bottom boundary layer and is due to bottom friction. The results in figure 14(a) show that the relative contribution of the bottom boundary layer to the total dissipation inside the current decreases with the increase in the Reynolds number. In the LR-F simulation, the values of ε^{23} in the tail region are 50%–100% larger at most streamwise locations, as compared with the HR-F case. The total dissipation over the whole length of the current ($x/H > 0$) is close to 30% larger in the LR-F simulation, once the regime where ε becomes close to constant is reached ($x_f/H > 10$).

Scale effects are much less significant in the simulations with obstacles. The distributions of ε^{23} are qualitatively and quantitatively similar over the whole length of the current (e.g. see figure 14b for the simulations with dunes). The difference in the values of ε between the low- and high-Reynolds-number simulations is less than

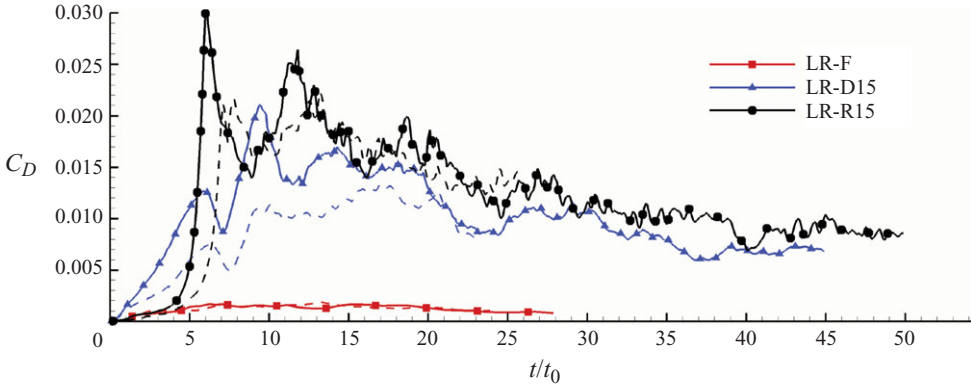


FIGURE 15. (Colour online) Temporal variation of the total drag coefficient over the region occupied by the first obstacle ($2.5 < x/H < 5.5$, solid line with symbols) and the third obstacle ($8.5 < x/H < 11.5$, dashed line) in the LR-F, LR-D15 and LR-R15 simulations. To facilitate the comparison of the total drag forces in the two regions, the curves were translated in time such that $t/t_0 = 0$ corresponds to the time the front of the current reaches $x/H = 2.5$ and $x/H = 8.5$, respectively.

5% beyond the initial stages of the slumping phase. This means that for $Re > 50\,000$ the flow is, to a large degree, controlled by the turbulent form drag induced by the obstacles, rather than by viscosity.

7. Drag forces

Figure 15 compares the total drag coefficient, C_D , induced by the passage of the bottom-propagating current over the streamwise region associated with the first ($2.5 < x/H < 5.5$) and third ($8.5 < x/H < 11.5$) obstacles for the LR-F, LR-R15 and LR-D15 simulations ($\lambda = 3H$, $L_3 = H$):

$$C_D = \frac{F_p + F_f}{0.5\rho u_b^2 L_3 \lambda}, \quad (7.1)$$

where F_p and F_f are the streamwise components of the pressure force acting on the front and back surfaces of the obstacle and the friction force, respectively. Both forces are calculated over a streamwise region of length λ , corresponding to the distance between one obstacle and the next.

The pressure drag is equal to zero in the LR-F simulation. The time variation of the drag coefficient is fairly independent of the position of the streamwise region of length $\lambda = 3H$ over which the friction drag is calculated. Here F_f increases until the front reaches the end of this streamwise region. It then remains approximately constant ($C_D \sim 0.0015$) for about $15t_0$, during which the head and dissipative wake regions propagate over the streamwise region. Then, F_f starts decreasing slowly.

The average levels of the friction drag in the LR-R15 and LR-D15 simulations (not shown) are comparable but lower than those in the LR-F simulation. Thus, in the simulations with obstacles of wavelength $\lambda = 3H$ conducted at $Re = 47\,800$, the pressure drag is about one order of magnitude higher than the friction drag. This confirms the important role played by the obstacles in the evolution of the current in cases LR-R15 and LR-D15.

The temporal variation of C_D over the streamwise region associated with rib 1 in the LR-R15 simulation is in many respects qualitatively similar to that observed by

Gonzalez-Juez *et al.* (2009) in a study of currents impinging on isolated obstacles. Here C_D increases exponentially during the impact stage, which lasts about $6t_0$ in case LR-R15. The increase in C_D is due to the interaction of the front with the bluff obstacle, which results in a strong pressure increase on the upstream face of the rib. The transient phase is characterized by large-scale temporal variations in the values of C_D . Similar to the 3-D simulation results of Gonzalez-Juez *et al.* (2009), C_D reaches a second maximum ($t \sim 12t_0$ in figure 15) during the transient phase. This second peak is induced by the decrease in the pressure on the downstream face of the rib, due to the increase in the strength of the recirculating vortex forming in between the heavier fluid from the splash that reaches the channel bottom and the downstream face of the rib. While in the case of an isolated obstacle C_D reaches fairly quickly a quasi-steady regime, in the present case the transient lasts for a much longer time. This is because of the passage of the backward-propagating jumps that form each time the front reaches a higher-rank obstacle. For example, the secondary dip of C_D around $t = 24t_0$ in figure 15 is associated with the passage of the backward jump forming at rib 2. The strength of the transient induced by the passage of the backward jumps decreases with the rank of the obstacle at which the jump originated. In a good approximation, the quasi-steady regime around rib 1 is reached by the time the backward jump originating at rib 3 passes rib 1. The temporal variation of C_D is fairly similar for the streamwise region associated with rib 3. The main difference is that the peak value of C_D at the end of the impact stage is smaller. This is because, by the time the front approaches rib 3, the front velocity is smaller and the mixing in the head region is larger as a result of the impact of the head of the current with the first two ribs.

The temporal history of C_D in the simulations with dunes and ribs of equal height is qualitatively similar during all the three phases. The largest quantitative difference occurs during the impact stage. As a result of the lower degree of bluntness of the dunes, the front deceleration is smaller and the pressure forces on the upslope face of the dune are weaker than those induced on the upstream face of the corresponding rib in case LR-R15. This explains the decrease observed in the peak value of C_D at the end of the impact stage by about 70 % with respect to case LR-R15. Moreover, the peak value of C_D in the simulation with dunes is not reached at the end of the impact stage, but rather during the transient stage. For a given obstacle rank, the maximum values of C_D during the transient phase in the simulation with dunes are only 30 %–50 % lower than the overall maximum value of C_D in the simulation with ribs. The values reached by C_D during the quasi-steady regime in the two simulations are close.

8. Mixing and entrainment

The mixing of a compositional current with the ambient flow can be quantified by computing the variation of the subvolume of the flow domain where the density/concentration exceeds a given threshold value that is larger than that of the ambient fluid, or it ranges between given bounds (see also Necker *et al.* 2005). The variation in the front position of the subvolume of the flow domain where $C > C_\theta$ can be used to quantitatively compare mixing among different simulations. For example, after non-dimensionalization with the initial volume of lock fluid, V_0 , the subvolume containing non-ambient fluid can be calculated as

$$V_\theta(x_f/H) = \frac{1}{V_0} \int_{\Omega} \alpha \, dV, \quad (8.1)$$

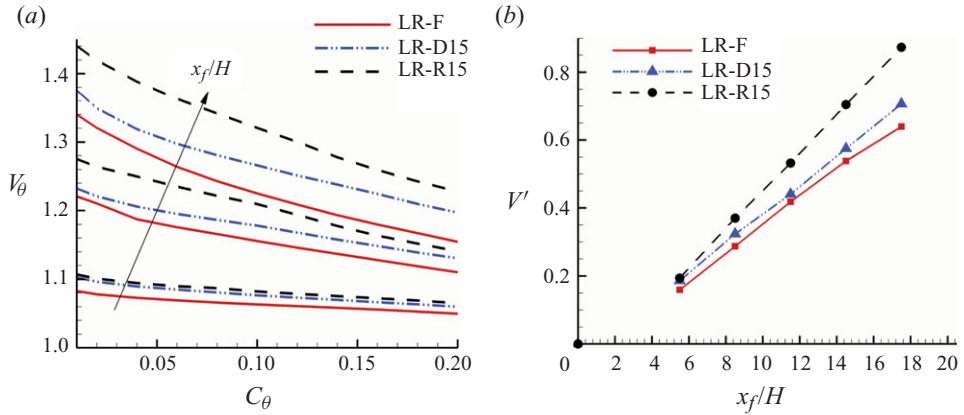


FIGURE 16. (Colour online) Mixing of the lock fluid and ambient fluid in the LR-F, LR-D15 and LR-R15 simulations. (a) The mixing is quantified by the normalized volume of mixed fluid $V_\theta(x_f/H)$ function of a threshold value of the concentration C_θ when the front is situated at $x_f/H = 5.5, 11.5$ and 17.5 . (b) The mixing is quantified by the normalized volume of mixed fluid V' ($0.02 < C < 0.98$) as a function of the front position.

where $\alpha = 1$ if $C > C_\theta$, $\alpha = 0$ if $C < C_\theta$ and C is the concentration field for a given value of the front position.

Figure 16(a) compares the variations of V_θ in the LR-F, LR-D15 and LR-R15 simulations for $0.01 < C_\theta < 0.2$. At $t = 0$, $V_\theta = 1$ for any value of C_θ ($0 < C_\theta < 1$). The higher degree of bluntness of the ribs induces the formation of a splash of heavier fluid and the trapping of a substantial amount of lock fluid downstream of the face of each rib overtaken by the current. This explains why, at a given front position, V_θ is the largest in the simulation with ribs. As expected, the smallest values of V_θ are observed for the flat-bed case in which most of the mixing occurs in the dissipative wake region. A comparison of the values of V_θ in the three simulations for relatively small (e.g. $C_\theta = 0.02$) and large (e.g. $C_\theta = 0.2$) threshold values of the concentration shows that the growth rate of the amount of mixed fluid within the bottom-propagating current depends strongly on the threshold value C_θ . In the three simulations, the degree of non-uniformity of the local concentration fields increases with time/front position, especially for $x_f/H > 11.5$. For small C_θ values, the values of V_θ in the simulation with dunes are closer to those in the simulation with a flat bed, while for large C_θ values, the values of V_θ in case LR-D15 are closer to those in the simulation with ribs. The cases with large-scale obstacles are more effective in increasing mixing over the whole depth of the bottom-propagating current compared with the case where the bottom surface is smooth. The larger values of V_θ observed in cases LR-R15 and LR-D15 compared with case LR-F for $C_\theta > 0.1$ are mainly due to the layer of mixed fluid that develops gradually in between two consecutive obstacles, as the backward-propagating jumps propagate over the tail of the current.

Figure 16(b) shows the variation of the (non-dimensional) volume of mixed fluid ($0.02 < C < 0.98$) in the channel $V'(x_f/H) = (\int_\Omega \alpha dV)/V_0$ with the front position, where $\alpha = 1$ if $0.02 < C < 0.98$ and $\alpha = 0$ if $C < 0.02$ or $C > 0.98$. As the lock and ambient fluids are separated at $t = 0$, $V' = 0$. Results show that past the initial stages of the slumping phase ($x_f/H > 5$), the variation of V' with time is close to linear in the simulations with dunes and ribs. The localized mixing associated with the splash of heavier fluid forming each time the front reaches a new rib accounts to a large

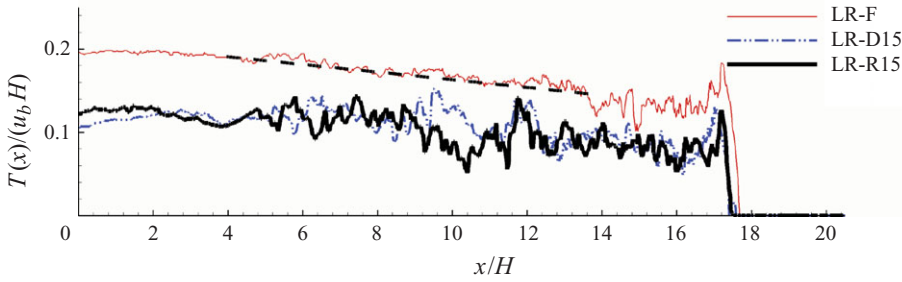


FIGURE 17. (Colour online) Total transport in the streamwise direction, $T(x)/(u_b H)$, in the LR-F, LR-D15 and LR-R15 simulations. The front is situated at $x_f/H = 17.5$. The straight dashed line approximates the slope of $T(x)$ over most of the tail region in case LR-F.

degree for the larger slope of V' in the LR-R15 case compared with the LR-D15 case. The trapping of ambient fluid, once the head propagates past the crest of a dune, is the main reason why the values of V' at a given front position are slightly larger in the LR-D15 case compared with the flat-bed case. Meanwhile, the rate of increase of V' in the two simulations is comparable.

Information on the entrainment along the current can be obtained from the streamwise variation of the total transport (volume flux) of fluid with density larger than that of the ambient fluid. Following Turner (1986) and Legg, Hallberg & Girton (2006), the non-dimensional total transport in the streamwise direction per unit width at a given time/front position is defined as

$$T(x) = \frac{1}{L_i} \int_A u \, dy \, dz, \tag{8.2}$$

where A is the part of the cross-section at $x = \text{constant}$, where C is larger than a threshold value, C_θ , and $L_i \cong L_3$ is the length of the interface ($C = C_\theta$) in the $x = \text{constant}$ plane. A value of 0.1 was used for C_θ in figure 17 to calculate $T(x)$ when $x_f/H = 17.5$ in the LR-F, LR-R15 and LR-D15 cases. The entrainment coefficient is defined as

$$\alpha_E(x) = \frac{1}{\bar{u}} \frac{dT(x)}{dx}, \tag{8.3}$$

where the mean streamwise velocity is $\bar{u}(x) = (1/A) \int_A u \, dy \, dz$. Simulation results show that in the flat-bed case, $T(x)$ is nearly constant close to the lock gate during the later stages of the slumping phase (e.g. for $x/H < 4$ in figure 17 for case LR-F), which indicates negligible entrainment. Then, the decay of T with x is close to linear over most of the tail region (e.g. $4 < x/H < 14$ in figure 17). On average, the total transport increases with x over the dissipative wake region. This is because the shedding of interfacial billows increases entrainment. On the basis of the experimental data of Ellison & Turner (1959), Turner (1986) proposed an empirical expression for the mean entrainment coefficient $\bar{\alpha}_E$ function of an overall Richardson number $Ri = g' \tilde{h} \cos \theta / \bar{U}^2 = (\tilde{h}/H) \cos \theta / (\bar{U}/u_b)^2$:

$$\bar{\alpha}_E = \frac{0.08 - 0.1 Ri}{1 + 5 Ri}. \tag{8.4}$$

For the flat-bed simulation ($\cos \theta = 1$), one can estimate the mean height of the current (\tilde{h}) and the mean streamwise velocity (\bar{U}) over the tail region where T decays linearly with x as $\tilde{h} \cong 0.5H$ and $\bar{U} \cong 0.33u_b$, respectively, for $x_f/H = 17.5$. The

average slope of $T(x)$ over the same region inferred from figure 17(a) is $-0.006u_b$. The corresponding value of the mean entrainment coefficient estimated using (8.3) is $\bar{\alpha}_E = -0.018$. The empirical formula (8.4) predicts $\bar{\alpha}_E = -0.016$ ($Ri \cong 5$). Despite the good agreement between the two values of $\bar{\alpha}_E$, one should interpret this result with care, as the experimental data of Ellison & Turner (1969) are limited to $Ri < 0.5$ and slopes larger than 10° . Turner's theory was developed for currents propagating over down slopes, where entrainment in the tail is more important. In fact, Turner (1986) made an important point that for currents propagating over horizontal bottoms, entrainment at the front is usually more important than that in the tail. Present results for the flat-bed case show that the volume flux of mixed fluid decreases in the streamwise direction over most of the tail region in the later stages of the slumping phase, which results in a negative entrainment coefficient. Also, Turner's theory is for flows in infinite domains, whereas in the present study we consider the case in which the channel height is only twice that of the gravity current. A direct comparison is even less relevant with the cases in which large-scale roughness elements are present at the bed, as his theory does not account for large-scale bottom roughness effects.

The cases with obstacles do not show a clear trend in the variation of $T(x)$ over the length of the current (figure 17). During the later stages of the slumping phase, the entrainment is negligible over the upstream part of the tail where the quasi-steady state was reached and the interface is close to horizontal. The large-scale variations of $T(x)$ are correlated with the regions where the head interacts with the crest of the obstacles (strong entrainment). Entrainment is also intensified close to the backward-propagating jumps, especially during the time when a jump interacts with the crest of an obstacle. In the simulations with ribs, $T(x)$ increases sharply over the head region in between the time when the front reaches the upstream face of the rib and when the splashed heavier fluid reaches the channel bottom and the head of the current regains its usual shape. This confirms that the formation of the splash for obstacles with high degree of bluntness induces strong mixing and entrainment at the head.

9. Summary and conclusions

The study investigated the physics of high-Reynolds-number ($Re_f > 10^4$) compositional Boussinesq gravity currents with a large volume of release in lock-exchange configurations, and their dynamic effects on 2-D obstacles (e.g. natural bedforms in alluvial channels in the form of dunes and flow retarding obstacles in the form of rectangular ribs used to slow down gravity currents) based on results of highly resolved LES. In the simulations with obstacles, the form drag was much larger than the friction drag. The study allowed quantifying the effect of the obstacle shape on the front velocity, the structure of the current, the energy balance, and qualitative and quantitative differences compared with the simpler, but much more widely studied, case of a gravity current propagating over a flat smooth surface. Additionally, LES conducted at $Re = 10^6$ helped to better understand the physics of finite-volume lock-release currents and their interactions with obstacles for flow conditions that are closer to the inviscid state that is often assumed in theoretical models, and to conditions encountered in practical applications in rivers, lakes and oceans.

Simulation results showed that currents propagating over an array of 2-D identical obstacles reach, under certain conditions, a slumping phase in which the front velocity is approximately constant. The front velocity is smaller than that reached by the same

gravity current propagating over a flat surface (no obstacles) and is a function of the relative degree of bluntness of the obstacles in the series (e.g. compared with the flat-bed case, the front velocity is smaller by 12 % for dunes and by 24 % for ribs of height $D=0.15H$ and wavelength $\lambda=3H$, and the current height is close to $H/2$). During this regime, the total kinetic energy increases with time proportional to $t^{1/3}$. This is different from the case of a gravity current with a high volume of release propagating over a flat bed, in which the kinetic energy increases linearly with time past the initial stages of the slumping phase. The conditions for a slumping phase to be present for an extended time, during which the front propagates over a large number of obstacles, depend on the magnitude of the drag force per unit streamwise length induced by the obstacles.

If the drag force per unit length increases due to an increase in the size of the obstacles or to a decrease in their spacing, then the slumping phase can be very short, or it may not be present at all. In contrast to the case of a current propagating over a flat surface for which the front velocity remains constant until the reflected disturbance reaches the front, the front velocity can start to decay with time due to the added drag force induced by the obstacles. A simulation conducted with densely spaced ribs in a long channel showed that after a short acceleration phase, the current transitioned directly to a turbulent drag-dominated regime in which the front velocity decays proportionally to t^β , with $\beta \sim -0.28$. Such a regime was previously shown to exist for gravity currents with a large volume of release propagating into a porous medium of uniform porosity occupying the whole channel, but not for the case in which the drag force acts only over the lower part of the bottom-propagating current. The present study showed that, as a result of the spatial differences in the distribution of the drag force acting on the gravity current, the shape of the current propagating over bottom-mounted obstacles (relatively horizontal interface until close to the head) is very different from the shape (interface with the ambient fluid is straight and inclined with respect to the horizontal) observed for currents propagating into a porous medium. In the latter case, the drag force is relatively uniformly distributed over the whole height of the current. Because of these differences, one does not expect β to be the same for the two types of gravity currents. However, the LES showed that after a certain time from the release of the lock gate, the flux of heavier fluid past the position of the gate becomes close to constant. This means that the theoretical model proposed by Hatcher *et al.* (2000) to estimate the decay of the front velocity for high-Reynolds-number gravity currents propagating in a porous medium in which the total volume of lock fluid increases linearly with time may apply. Indeed, the value of β predicted by LES ($\beta = -0.28$) was close to that predicted by the theoretical model ($\beta = -0.25$). Simulation results also showed that, after the flux becomes constant and the front starts decelerating, the kinetic energy starts decaying linearly with time and with the front position. This is consistent with the current reaching a drag-dominated regime in which the front velocity decays continuously in time.

For gravity currents with a large volume of release for which the slumping phase lasts a relatively long time, the structure of the flow in the head and dissipative wake was found to change dramatically as a result of the presence of the obstacles compared with the flat case. A strong jet-like flow formed downstream of the top or crest of each obstacle, shortly after the front started moving away from the obstacle. For the obstacles considered in the simulations ($D=0.15H$, $\lambda=3H$), the flow became supercritical in the region of strong flow acceleration, in which the higher-density fluid inside the jet-like flow plunges towards the lower regions of the bed

surface, at least for the obstacles situated close to the front. Significant changes were also observed over the tail region. The stably stratified tilted interface, depleted of large-scale eddies, which develops behind the dissipative wake in the flat-bed simulations, was absent in the simulations with obstacles. Rather, at sufficiently large times after the passage of the backward-propagating hydraulic jumps forming at the crest of each obstacle when the front reaches that obstacle, a layer of varying height containing mixed fluid developed between the regions containing heavier and lighter fluid. The top of the mixed fluid layer was close to horizontal at large distances behind the front. The passage of the hydraulic jumps also affected the time variation of the total drag force induced over the region associated with a certain obstacle in the series. Results showed that the transient phase lasts for a significantly longer time compared with the case of an isolated obstacle. For the simulations with obstacles of height of $0.15H$, the quasi-steady regime around obstacle i in the series started when the backward jump originating at obstacle $i + 2$ reached obstacle i .

As expected, for a given position of the front, the amount of mixed fluid was larger in the simulations with obstacles and was a function of the degree of bluntness of the obstacles. Result showed that, past the initial stages of the slumping phase, the variation of the volume of mixed fluid with time is close to linear in the simulations with obstacles. The simulation conducted with a flat horizontal bed showed that the average volume flux of mixed fluid decreases in the streamwise direction over most of the tail region of the current. In contrast, the simulations with obstacles showed that though the volume flux of mixed fluid is subject to larger-scale oscillations over most of the tail region, the average level of the volume flux does not vary significantly in the streamwise direction.

The case of gravity currents with a small volume of release propagating over an array of obstacles is expected to introduce a new level of complexity compared with that of a flat horizontal bottom (e.g. see numerical studies of Hallez & Magnaudet 2009 and Ooi *et al.* 2009 for the latter case). In the case obstacles are present at the channel bottom, the current is expected to transition first to the buoyancy–inertia phase and then to the drag-dominated regime. Not much is known about the changes in the structure of the current and the variations of the main parameters characterizing its evolution during these two regimes for gravity currents propagating over obstacles. The present model is being applied to investigate this case, which is very relevant for applications in river and ocean engineering, in which gravity currents generally propagate over a rough bed containing large-scale roughness elements, as well as for applications related to snow avalanches whose propagation may be accompanied by disastrous damage. Furthermore, in the presence of rotation, novel mechanisms can arise for gravity currents propagating over arrays of obstacles. For example, Darelius & Wahlin (2007) and Darelius (2008) investigated geostrophic plumes encountering a ridge on a continental slope. They developed a simplified model and performed laboratory experiments to show that the interaction of the plume with the ridge can lead to enhanced downslope transport of dense fluid, via a process termed ‘topographic steering’.

We gratefully acknowledge the National Center for High Performance Computing (NCHC) in Taiwan, in particular Dr W. F. Tsai, for providing substantial computer time as part of the collaborative programme between NCHC and IIHR–Hydroscience and Engineering. This paper was written while G.C. was on sabbatical leave at the Laboratory of Hydraulics, Hydrology and Glaciology (VAW) at ETH Zurich. He

thanks Professor W. Hager and the other researchers at VAW for their support. E.M. acknowledges financial support through NSF grant CBET-0854338.

Supplementary movies are available at journals.cambridge.org/flm.

REFERENCES

- ALEXANDER, J. & MORRIS, S. 1994 Observations on experimental, non-channelized, high-concentration turbidity currents and variations in deposits around obstacles. *J. Sedim. Res. A* **64** (4), 899–909.
- DE ANGELIS, V., LOMBARDI, P. & BANERJEE, S. 1997 Direct numerical simulation of turbulent flow over a wavy wall. *Phys. Fluids* **9**, 2429–2442.
- ARMI, L. 1986 The hydraulics of two flowing layers with different densities. *J. Fluid Mech.* **163**, 27–58.
- BENJAMIN, T. B. 1968 Gravity currents and related phenomena. *J. Fluid Mech.* **31**, 209–248.
- BONOMETTI, T., BALACHANDAR, S. & MAGNAUDET, J. 2008 Wall effects in non-Boussinesq density currents. *J. Fluid Mech.* **616**, 445–475.
- CANTERO, M. I., LEE, J. R., BALACHANDAR, S. & GARCIA, M. H. 2007 On the front velocity of gravity currents. *J. Fluid Mech.* **586**, 1–39.
- CHANG, K. S., CONSTANTINESCU, G. & PARK, S.-O. 2006 Analysis of the flow and mass transfer processes for the incompressible flow past an open cavity with a laminar and a fully turbulent incoming boundary layer. *J. Fluid Mech.* **561**, 113–145.
- CHANG, K., CONSTANTINESCU, G. & PARK, S. O. 2007 The purging of a neutrally buoyant or a dense miscible contaminant from a rectangular cavity. Part II: The case of an incoming fully turbulent overflow. *ASCE J. of Hydr. Engrg* **133**(4), 373–385.
- DARELIUS, E. 2008 Topographic steering of dense overflows: laboratory experiments with V-shaped ridges and canyons. *Deep-Sea Res. I* **55**, 1021–1034.
- DARELIUS, E. & WAHLIN, A. 2007 Downward flow of dense water leaning on a submarine ridge. *Deep-Sea Res. I* **54**, 1173–1188.
- DJENIDI, L., ELAVARASAN, R. & ANTONIA, R. A. 1999 The turbulent boundary layer over transverse square cavities. *J. Fluid Mech.* **395**, 271–294.
- ELLISON, T. H. & TURNER, J. S. 1959 Turbulent entrainment in stratified flows. *J. Fluid Mech.* **6**, 423–448.
- ERMANYUK, E. V. & GAVRILOV, N. V. 2005a Interaction of an internal gravity current with a submerged circular cylinder. *J. Appl. Mech. Tech. Phys.* **46** (2), 216–223.
- ERMANYUK, E. V. & GAVRILOV, N. V. 2005b Interaction of an internal gravity current with an obstacle on the channel bottom. *J. Appl. Mech. Tech. Phys.* **46** (4), 489–495.
- FANNELÓP, T. K. 1994 *Fluid Mechanics for Industrial Safety and Environmental Protection*. Elsevier.
- GONZALEZ-JUEZ, E. & MEIBURG, E. 2009 Shallow water analysis of gravity current flows past isolated obstacles. *J. Fluid Mech.* **635**, 415–438.
- GONZALEZ-JUEZ, E., MEIBURG, E. & CONSTANTINESCU, G. 2009 Gravity currents impinging on bottom mounted square cylinders: flow fields and associated forces. *J. Fluid Mech.* **631**, 65–102.
- GONZALEZ-JUEZ, E., MEIBURG, E., TOKYAY, T. & CONSTANTINESCU, G. 2010 Gravity current flow past a circular cylinder: forces and wall shear stresses and implications for scour. *J. Fluid Mech.* **649**, 69–102.
- HALLEZ, Y. & MAGNAUDET, J. 2008 Effects of channel geometry on buoyancy-driven mixing. *Phys. Fluids* **20**, 053306.
- HALLEZ, Y. & MAGNAUDET, J. 2009 A numerical investigation of horizontal viscous gravity currents. *J. Fluid Mech.* **630**, 71–91.
- HALLWORTH, M. A., HUPPERT, H. E., PHILLIPS, J. C. & SPARKS, S. R. 1996. Entrainment into two-dimensional and axisymmetric turbulent gravity currents. *J. Fluid Mech.* **308**, 289–311.
- HÄRTEL, C., MEIBURG, E. & NECKER, F. 2000 Analysis and direct numerical simulation of the flow at a gravity-current head. Part 1. Flow topology and front speed for slip and no-slip boundaries. *J. Fluid Mech.* **418**, 189–212.

- HATCHER, L., HOGG, A. J. & WOODS, A. W. 2000 The effects of drag on turbulent gravity currents. *J. Fluid Mech.* **416**, 297–314.
- HOPFINGER, E. J. 1983 Snow avalanche motion and related phenomena. *Annu. Rev. Fluid Mech.* **15**, 47–76.
- HUPPERT, H. & SIMPSON, J. E. 1980 The slumping of gravity currents. *J. Fluid. Mech.* **99**, 785–799.
- IKEDA, T. & DURBIN, P. A. 2002 Direct numerical simulation of a rough wall channel flow. *Report No. TF-81*. Flow Physics and Computation Division, Department of Mechanical Engineering, Stanford University, Stanford, California, USA.
- JIMENEZ, J. 2004 Turbulent flows over rough walls. *Annu. Rev. Fluid Mech.* **36**, 173–196.
- JOHANNESSON, T., LIED, K., MARGRETH, S. & SANDERSON, F. 1996 An overview of the need for avalanche protection measures in Iceland. *Report Prepared for the Icelandic Ministry for the Environment and Local Authorities in Towns Threatened by Avalanches*. Reykjavik, Iceland.
- KEULEGAN, G. H. 1957 An experimental study of the motion of saline water from locks into fresh water channels. *U.S. Natl Bur. Stand. Rep.* 5168.
- KNELLER, B., BENNETT, S. J. & MCCAFFREY, W. D. 1999 Velocity structure, turbulence and fluid stresses in experimental gravity currents. *J. Geophys. Res. Oceans* **104** (C3), 5381–5391.
- LANE-SERFF, G. F., BEAL, L. M. & HADFIELD, T. D. 1995 Gravity current flow over obstacles. *J. Fluid Mech.* **292**, 39–53.
- LEGG, S., HALLBERG, R. W. & GIRTON, J. B. 2006 Comparison of entrainment in overflows simulated by z -coordinate, isopycnal and non-hydrostatic models. *Ocean Model.* **11**, 69–97.
- LEONARDI, S., ORLANDI, P., DJENIDI, L. & ANTONIA, R. A. 2003 Direct numerical simulations of turbulent channel flow with transverse square bars on one wall. *J. Fluid. Mech.* **491**, 229–238.
- LIAPIDEVSKII, V. Y. 2004 Mixing layer on the lee side of an obstacle. *J. Appl. Mech. Tech. Phys.* **45** (2), 199–203.
- MAHESH, K., CONSTANTINESCU, G. & MOIN, P. 2004 A numerical method for large eddy simulation in complex geometries. *J. Comput. Phys.* **197**, 215–240.
- MEIBURG, E. & KNELLER, B. 2010 Turbidity currents and their deposits. *Annu. Rev. Fluid Mech.* **42**, 135–156.
- MIERLO, M. C. & DE RUITER, J. C. 1988 Turbulence measurements over artificial dunes. *Rep. Q789*. Delft Hydraulics Laboratory, Delft, The Netherlands.
- NECKER, F., HÄRTEL, C., KLEISER, L. & MEIBURG, E. 2002 High-resolution simulations of particle-driven gravity currents. *Intl J. Multiphase Flow* **28**, 279.
- NECKER, F., HÄRTEL, C., KLEISER, L. & MEIBURG, E. 2005 Mixing and dissipation in particle-driven gravity currents. *J. Fluid Mech.* **545**, 339–372.
- OOI, S. K., CONSTANTINESCU, S. G. & WEBER, L. 2007a A numerical study of intrusive compositional gravity currents. *Phys. Fluids* **19**, 076602, doi:10.1063/1.2750672.
- OOI, S. K., CONSTANTINESCU, G. & WEBER, L. J. 2007b 2D Large Eddy Simulation of lock-exchange gravity current flows. *ASCE J. of Hydr. Engrg* **133**(9), 1037–1047.
- OOI, S. K., CONSTANTINESCU, S. G. & WEBER, L. 2009 Numerical simulations of lock exchange compositional gravity currents. *J. Fluid Mech.* **635**, 361–388.
- OZGOKMEN, T. M. & FISHER, P. F. 2008 On the role of bottom roughness in overflows. *Ocean Model.* **20**, 336–361.
- OZGOKMEN, T. M., FISHER, P. F., DUAN, J. & ILIESCU, T. 2004 Entrainment in bottom gravity currents over complex topography from three-dimensional nonhydrostatic simulations. *Geophys. Res. Lett.* **31**, L13212, doi:10.1029/2004GL0200186.
- PAWLAK, G. & ARMI, L. 2000 Mixing and entrainment in developing stratified currents. *J. Fluid Mech.* **424**, 45–73.
- PIERCE, C. D. & MOIN, P. 2001. Progress-variable approach for large-eddy simulation of turbulent combustion. *Mech. Engng Dept. Rep. TF-80*. Stanford University, California, USA.
- PIERCE, C. D. & MOIN, P. 2004 Progress-variable approach for large-eddy simulation of non-premixed turbulent combustion. *J. Fluid Mech.* **504**, 73–97.
- ROTTMAN, J. W. & SIMPSON, J. E. 1983 Gravity currents produced by instantaneous releases of a heavy fluid in a rectangular channel. *J. Fluid Mech.* **135**, 95–110.

- ROTTMAN, J. W., SIMPSON, J. E., HUNT, J. C. R. & BRITTER, R. E. 1985 Unsteady gravity current flows over obstacles: some observations and analysis related to the phase II trials. *J. Hazard. Mater.* **11**, 325–340.
- SHIN, J., DALZIEL, S. & LINDEN, P. F. 2004 Gravity currents produced by lock exchange. *J. Fluid Mech.* **521**, 1–34.
- SIMPSON, J. E. 1997 *Gravity Currents: In the Environment and the Laboratory*, 2nd edn. Cambridge University Press.
- TANINO, Y., NEPF, H. M. & KULIS, P. S. 2005 Gravity currents in aquatic canopies. *Water Resour. Res.* **41**, W12402.
- TURNER, J. S. 1986 Turbulent entrainment: the development of the entrainment assumption, and its application to geophysical flows. *J. Fluid Mech.* **173**, 431–471.